

This 90 page document is my research advisor's PhD dissertation.

Click [here](#) to skip to the contributions I, Srivishal Sudharsan, made.

INFERRING THE COMPOSITIONS AND INTERIOR STRUCTURES OF SMALL

PLANETS By

David R. Rice

Bachelor of Arts – Integrated Science
Bachelor of Arts – Physics and Astronomy
Bachelor of Arts – Earth and Planetary Sciences
Northwestern University
2016

Master of Science – Astronomy
University of Nevada, Las Vegas
2019

A dissertation submitted in partial fulfillment
of the requirements for the

Doctor of Philosophy – Astronomy

Department of Physics and Astronomy
College of Sciences

The Graduate College

University of Nevada, Las Vegas

May 2023

Abstract

Although there are now over 10,000 confirmed and candidate extrasolar planets, accurate masses and radii have been determined for around 200 planets of less than 10 Earth-masses. This number will grow exponentially over the next decade as extreme precision radial velocity spectrographs see first light. The densities of small planets hint at a diverse range of compositions for terrestrial worlds from super-Mercuries to super-Ganymedes. Uncertainty in density is as low as 3% in the Trappist-1 system. To determine composition from observed parameters, the community uses a variety of interior structure models. Underlying these models are multiple computational techniques, numerous experimental measurements and theoretical estimates of the equations of state for planet-building materials, and differing treatments of temperature. I present MAGRATHEA, an open-source interior structure solver which can be customized to user-defined planet models for reproducible characterizations. Our code features adaptable phase diagrams for the core, mantle, hydrosphere, and atmosphere and transparent storage for equations of states. I demonstrate how I use MAGRATHEA in concert with high-pressure physicists to improve our interior models and with observational data to characterize planets. While previous works have looked at how models affect mass-radius relationships, I carry through uncertainties to the characterization of small planets with known density. I show how observed, model, and

experimental uncertainties affect inferences of water mass fraction in the Trappist-1 system. The Earth's composition and interior structure can soon be understood in the greater context of exoplanet diversity.

iii Acknowledgements

My advisor, Dr. Jason H. Steffen, has supported and motivated me throughout this work. I thank him for his many years of advising. I thank Dr. Chenliang Huang for his partnership in developing our interior code. I acknowledge the valuable discussions and feedback from my research group— Dr. Anna Childs, Cody Shakespeare, Nick Juliano, Stanley Baronett, Bo Royer, Abigail Graham, and Noah Ferich along with many other colleagues at UNLV and across the world. I acknowledge support from the Department of Physics and Astronomy, Nevada Center for Astrophysics, and the College of Sciences at the University of Nevada, Las Vegas. This work was supported by a 2018 Graduate Fellowship from The Nevada Space Grant Consortium, UNLV Graduate Assistantships, the Graduate College Rebel Research and Mentorship Program, and a 2023 UNLV President's Foundation Graduate Research Fellowship. Computational resources were provided by the Cherry Creek Cluster at the UNLV National Supercomputing Institute.

I am forever thankful for the love and support of my parents, sister, and family in-law. My wife, Nicole Rice, is the brightest star in my life and has been the foundation that made the completion of this work possible.

iv
Table of Contents

Abstract	
. iii Acknowledgements	
. iv List of Tables	
. vii List of Figures	
. viii	
Chapter 1 Introduction	
. 1 1.1 Small Exoplanet Demographics	
. 1 1.2 Main Components of Small Planet Interiors	
. 5	
1.2.1 Cores	
. 6 1.2.2 Mantles	
. 7 1.2.3 Volatile Layers	
. 8	
1.3 Planet Interior Solvers	
. 9 1.3.1 Applications to Small Planets	
. 12 1.4 Overview	
. 13	
Chapter 2 MAGRATHEA: an Open-Source Spherical Symmetric Planet Interior Structure Code 14 2.1 Background	
. 14 2.2 Interior Structure Solver	
. 16	
2.2.1 Phase Diagrams	
. 18 2.2.2 Equation of State Formulae	
. 20 2.2.3 Tabulated Equation of State	
. 26 2.2.4 User-Defined Function	
. 26	
2.3 Overview of the Code Structure	

27	2.3.1 Solver	27
27	2.3.2 Simplified Two Layer Mode	29
29	2.3.3 Phase Diagram	30
30	2.3.4 Implementation	31
31	2.3.5 Core/Iron	33
33	2.3.6 Mantle/Silicate	33
33	2.3.7 Hydrosphere/Water	34
34	2.3.8 Atmosphere/Gas	36
36		
38	2.4 Known Limitations	38
38	2.5 Test Problems and Utility	39
39	2.5.1 One-Earth Mass and Comparison with	39
39	ExoPlex	41
41		

v

43	2.5.3 Uncertainty from Equation of State	43
43	2.5.4 Ternary Diagram	45
45	2.5.5 Ternary with Atmosphere	49
49	2.6 EoS Storage Structure	49
49	2.7 Modify a Built-In EoS in Runtime	54
54	2.8 Summary	56
56		

57	Chapter 3 Further MAGRATHEA Developments	57
57	3.1 Background	57
57	3.2 Composition Finder	58
58	3.3 3D Planet Rendering	63
63	3.4 Summary	67
67	and Future Development	

71	Chapter 4 Advancements in EoS and Expansion of EoS Library	71
71	4.1 Background	71
71	4.2 New Water-Ice Experimental EoS	73
73	4.3 Core Iron EoS	76
76	4.4 FCC and	
	BCC Iron	79
79	4.5 Upper Mantle Materials	81
81	4.6 Summary and Future Work	85
85		

89	Chapter 5 Characterizing the Composition of Planets	89
89	5.1 Background	

.....	89	5.2 K2-138 Planetary System	
.....	90	5.3 Water Worlds and Super	
Earths	97	5.4	
TRAPPIST-1 Planets from Formation Models			
.....	102	5.5 Summary	
.....	105		
Chapter 6 Uncertainties in Inferences of Internal Structure			
.....	107	6.1 Background	
.....	107	6.2 Graphical Representations	
.....	109	6.3 TRAPPIST-1 System	
Default Compositions	113		
6.3.1 T1f Default Model.			
.....	115	6.4 T1f Uncertainties.	
.....	118	6.4.1 Observational	
.....	118	6.4.2 Model Choices	
.....	122	6.4.3 Experimental	
.....	124	6.5	
Summary			
.....	127		
Chapter 7 Conclusion			
.....	128	References	
.....			
.....	132	Curriculum Vitae	
.....			
.....	146		

vi List of Tables

2.1 List of status information of the planet profile object	
.....	29
2.2 EoS parameters for Smith et al. (2018), Sakai et al. (2016), and	
Grande et al. (2022) with uncertainty and the uncertainty in radius for a 10 M _⊕	
single-layer planet from uncertainty in EoS parameters.	
.....	44
2.3 Index for types of isothermal EoS formulae	
.....	50
2.4 Temperature profile option ..	
.....	51
2.5 List of EoS	
parameters	
.....	52
3.1 Inputs for the composition finder with line numbers in <i>main.cpp</i>	
.....	59

4.1 Frank et al. (2004) and Grande et al. (2022) best fit EoS parameters. The Zeng et al. (2016) paper uses a different parameterization for their EoS (see Zeng & Sasselov 2013).	75
5.1 Core mass fraction (cmf), mantle mass fraction (mmf), water mass fraction (wmf) and resulting radius for the T1 planets using the average bulk compositions from the simulated planets. We report these properties for starting bodies with a wmf of 0.20 and 0.50.	103
6.1 2,500 samples of mass and radius were generated for each row of properties and with median values of Trappist-1f. Uncertainty in wmf shown at 0.33 and 0.60 r-cmf. Final column is uncertainty in cmf at 0% wmf.	118
6.2 2,500 samples of radius were generated from skewed distributions and paired with with masses drawn from a Gaussian with $1.039 \pm 0.31 M_{\oplus}$. <i>Skew</i> is the Fisher Pearson coefficient of skewness. <i>Earth W%</i> is the wmf % at a given 0.33 RCM.	120

1.1 The bulk density with planet mass of confirmed exoplanets with both accurately determined mass and radius. Null-albedo equilibrium temperature of the planets are represented by color. Three lines of constant interior structure are shown for 100% core, 100% mantle, and 100% water planets.	2
1.2 The works that inform the planet interior model in two recent planet interior works— Acuna et al. (2021) and Dorn & Lichtenberg (2021). Tree structure shows previ- ~ ous works the models are built upon which are not all cited in the top-level paper. Works color coded by layer they inform. Works in figure: Brugger et al. (2016;	

2017); Sotin et al. (2007); Valencia et al. (2007b); Frank et al. (2004); Duffy et al. (1995); Bouhifd et al. (1996); Vacher et al. (1998); Anderson et al. (1991); Lide (2002); Fei et al. (1993); Poirier (2000); Stixrude & Lithgow-Bertelloni (2005); Tsuchiya et al. (2004); Williams & Knittle (1997); Uchida et al. (2001); Mousis et al. (2020); Mazevet et al. (2019); Baez & Clancy (1995); Tulk et al. (1997); ' Tchijov (2004); Shaw (1986); Feistel & Wagner (2006); Bezacier et al. (2014); Dunaeva et al. (2010); Dorn et al. (2015; 2017b); Hakim et al. (2018); Miozzi et al. (2020); Dorogokupets et al. (2017); Ichikawa & Tsuchiya (2020); Kuwayama et al. (2020); Anzellini et al. (2013); Stixrude (2014); Connolly (2009); Stewart et al. (2020); Faik et al. (2018); Melosh (2007); Belonoshko et al. (2005a); Stixrude (2014; 2012); Haldemann et al. (2020); Journaux et al. (2020); Wagner & Pruß (2002); Brown (2018); Gordon & McBride (1994); McBride & Gordon (1996); Mazevet et al. (2019).
 11

- 2.1 A schematic overview of MAGRATHEA. Showing an example input, *left*, of a 1.1 M_⊕ planet with 0.4 M_⊕ core, 0.4 M_⊕ mantle, and 0.3 M_⊕ hydrosphere. The planet is not in thermal equilibrium with a surface temperature of 300 K and jumps in temperature across boundary layers of 600 K and 1200 K. *Center*, shows MAGRATHEA's four input layers with cartoons of phase diagrams defined for each layer with an EoS chosen for each phase. Default phase diagrams shown in Fig. 2.2. *Right*, shows the pressure and temperature with enclosed mass. The radius at boundaries and the planet radii is also shown. 19
- 2.2 Default phase diagrams for hydrosphere, mantle, and core layers. EoS and phase transitions from a variety of sources detailed in Sec. 2.3.4. Type of EoS fitting equation shown from Sec. 2.2.2. Additionally, the parameters for mantle EoSs are shown, *middle*. The phase diagrams and choice of EoS can be customized by the user. *N.I.* is *not implemented*. The atmosphere layer also has a phase function, but our default is ideal gas at all pressure and temperatures, see Sec. 2.3.8 20

- 2.3 *Top*, mass-radius relationship for planets with 100 per cent of mass in either the core, mantle, or hydrosphere demonstrating many of the EoSs implemented in MAGRATHEA. *Bottom*, percent difference in final planet radii compared to our selected "default" EoSs for water (*top*), mantle (*middle*), and core (*bottom*). Table lists the major components of each model with 300 K surface temperature unless designated with a "-2000". Near the surface, water planets have water and Ice VI, and hot mantle planets have silicate melt. 32
- 2.4 Density, pressure, and temperature verses radius solution for a two-layer, one Earth-mass planet with 33 per cent by mass core. The three models shown are *Ma grathea Default* with hcp-Fe core (Smith et al. 2018) and Brg/PPv mantle (Oganov & Ono 2004; Sakai et al. 2016), *Magrathea Adjusted* with Fe-Si alloy core (Wicks et al. 2018) and PREM mantle (Zeng et al. 2016) and a

temperature discontinuity, and the default settings in *ExoPlex*. *Magrathea Default* is set to 300 K at the surface while *ExoPlex* suggests a 1600 K mantle. Temperature is solved through out *Magrathea Default* and in *ExoPlex*'s mantle. *Magrathea* returns no change in temperature when a phase does not have temperature parameters available while *ExoPlex* returns zero Kelvin. The planet's radius and the average run time over 100 integrations is listed in the legend. 40

2.5 Plot of run time, *top*, and of run time divided total number of steps, *bottom*, for our default model across six planet masses and four compositions: 100% core, 30% core 70% mantle, 30% core 40% mantle 30% water, and 30% core 40% mantle 29.99% water 0.01% H/He atmosphere with 300 K surface temperature. The last set of planets, *orange*, have 30% core, 70% mantle, and surface temperature of 2000 K. The run time is the average time measured across 100 runs. Sizes of the markers are proportional to the planet radius. 42

2.6 *Left*, ternary diagram where the axes are the percentage of mass in a core, mantle, and water/ice layer. The radius in Earth radii is shown by the color scale for 5151, one Earth-mass planets at integer percentages with our default model. Color map is interpolated between the simulations. *Right*, plot of *MAGRATHEA*'s run time for each planet. *Middle*, histogram of run time on a log-log scale showing mean time of 1.014 seconds. Ternary plots are generated with the python-ternary package by Harper et al. (2015) with colormaps from Van der Velden (2020). 46

2.7 Core-Mantle-Water mass percentage ternary plot with colored contours of constant radius for one Earth-mass planets. Four types of planets, represented by the line style, are calculated: one with no atmosphere and three with 0.01 per cent of their mass in an atmosphere layer. The atmosphere mass was subtracted equally from both the mantle and core to keep total mass equal to one Earth-mass. The three atmospheres have varying mean molecular weight: CO₂ with 44 g mol⁻¹, H₂O with 18 g mol⁻¹, and H/He mixture with 3 g mol⁻¹. 48

3.1 *Left*, a Blender rendering of an Earth-like planet with 32.5% of mass in the core with changes in mineralogy marked by changes in color in the interior. *Right*, in *blue* the density, pressure, and temperature of the Earth-like planet compared to a isothermal profile for PREM mantle and hcp-iron core. The radius of discontinuities in density on *top right* correspond with changes in color in 3D *left*. 65

3.2 *Top*, 100% mantle planets. *Bottom*, planets with significant hydrospheres. *Top left*, planet that is 1 M_⊕ and 1.07 R_⊕ surface of 300 K. *Top right*, planet that is 1.1 M_⊕ and 1.1 R_⊕ and surface of 1000 K. The second planet's temperature leads to a wds layer shown in green/grey under the olivine layer. *Bottom left*, planet that is 0.63 M_⊕ and 0.97 R_⊕ with 42% core. *Bottom, right*, planet that is 0.56 M_⊕ and 0.99 R_⊕ with 35% core.

.....	66
3.3 The density inside the Earth-like planet in Fig. 3.1. The density increases fairly linearly in the mantle with density jumps in the liquid outer core and solid inner core. The current method does not resolve the upper mantle materials well. Colors are rendered differently in Blender based on lighting and other “material properties” of the 3D sphere so may not correspond exactly to the colorbar. . . .	68
4.1 The density with depth of two $1 M_{\oplus}$ planets made of pure gold and platinum. This is for illustrative purposes as planets are not made out of pure gold and platinum. Inset shows percent difference between the two planets’ densities as a function of depth.	72
4.2 Impact of ice EoS measurements on inferences of minimum atmospheric weight for K2-18b. The three EoS shown are EOS I: Grande et al. (2022), EOS II: Zeng et al. (2016), EOS III: Frank et al. (2004). Lines show the fraction of planet mass in an atmosphere needed to reproduce the radius of K2-18b across a range of likely masses. Planets are modeled as pure water with a 3.0 g/mol ideal gas atmosphere and a equilibrium temperature of 255 K. The grey areas show the one and two sigma mass bounds of K2-18b. Planets with varying atmosphere are run at each half step in sigma. The shaded regions show the atmosphere needed to reproduce the radius of K2-18b to within one sigma for each EoS. One error bar is shown at $8.63 M_{\oplus}$. Planet parameters from Benneke et al. (2019).	77
4.3 Impact of iron’s bulk modulus on the inferred water mass fraction of Trappist-1 f at median value of mass and radius assuming an earth like core to mantle ratio. The lower bulk modulus of Smith et al. (2018) leads to the planet needing more water to match observed characteristics. Planet parameters from Agol et al. (2021).	78
4.4 Gruneisen parameter as a function of density, “ <i>blue</i> , with error, <i>light blue</i> , from Fig. 2b in Smith et al. (2018). Relationship with best fit parameters for Eq. 2.13 shown in <i>orange</i>	80
4.5 <i>Left</i> , this graph shows a mass-radius plot with comparison between planets with low pressure iron and without and with different surface temperatures. <i>Right</i> , this graph shows the percent difference between the planets with low pressure iron and without.	82
4.6 A phase diagram showing temperature-pressure profiles for the mantles of three masses of planets with an Earth-like 32.5% of their mass in the core and a mantle adiabat which starts at 2000 K. A diamond marks the central temperature and pressure for each planet mass. The planets pass through many phases of magnesium silicates. Depths shown for the $1 M_{\oplus}$ Earth-like planet.	84
4.7 <i>Left</i> , a comparison of the output radius of the models based on given 100% mantle planetary masses. <i>Right</i> , the graph displays the percentage differences between two models given in legend.	

..... 85

x

- 4.8 A phase diagram showing temperature-pressure profiles for the cores of planets from Fig. 4.6. Planets are simulated with a 1200 K increase in temperature at the CMB. All three cores are pure hcp Iron, but the melt curve for a iron sulfur mix is also plotted. 88

- 5.1 Mass-radius diagram with the radius and mass estimates of K2-138's planets. These estimates were pulled from normal distributions centered on the values from Lopez et al. (2019), with standard deviations equal to the uncertainties. We over plot composition curves of Earth-like (solid), 1% H/He atmosphere (short dash), and 100% water (long dash). We find that K2-138b is consistent with an Earth-like and terrestrial compositions, but that planets c-f require at least 1% H/He envelopes to satisfy their densities. 92

- 5.2 Ternary diagram where the axes are the percentage of mass in a core, mantle, and hydrosphere. Background thin lines are solutions from MAGRATHEA to 1000 samples of each planet's observed mass and radius. The wmf needed to match the observed radius is found across core:mantle ratio. Large solid lines of the corresponding planet color is the median wmf while dashed lines are the 1σ bounds. K2-138b (*blue*) is the only planet where all 1000 samples have non-atmosphere solutions. The median sample of K2-138c (*green*) and d (*orange*) require an atmosphere and only the -1σ bound of wmf is shown. Grey dashed line shows a constant Earth-like core to mantle ratio. 95

- 5.3 The water and atmosphere mass needed to match 100 and 1000 observed samples of mass and radius. The remaining mass is split 33:67 into the core and mantle. Thin background lines are solutions to each sample. Solid thick lines are the mean and 1σ bounds of samples with solutions at the given water mass. An isentropic temperature profile is used with the surface temperature set to the equilibrium temperature from Lopez et al. (2019). The statistics for K2-138b are only calculated up to when half of the samples have solutions requiring more than $10^{-4}\%$ atmosphere mass. 186 samples of K2-138b are too dense to require an atmosphere mass of more than $10^{-4}\%$ 96

- 5.4 Water-Mantle-Core mass ternary diagram with interior solutions to GJ 1252b from mass and radius in Luque & Palle (2022). *Red*, shows the median and $1-\sigma$ bounds of valid solutions. The most-probable water mass fraction is below 50% for all r-cmf. 99

- 5.5 *Left*, nine planets reanalyzed by Luque & Palle (2022) on a mass-radius diagram. *Curves* for Earth-Like (32.5% mantle, 67.5% core) and Water-World (50% water, 50% mantle) interiors shown. *Right*, plot of bulk density normalized to Earth and uncompressed density. The planets are modeled with MAGRATHEA to find the uncompressed density with uncertainty. Trappist-1 f and Solar

System bodies also shown.	101
-----------------------------------	-----

6.1 The two primary representations of planet composition in this chapter. <i>Left</i> , a water-mantle-core mass ternary diagram. <i>Right</i> , a water mass fraction with r-cmf (refractory core mass fraction) plot. Helpful definitions are supplied on the plot for the axes. A line of solutions for three-layer internal structure for a planet of given mass and radius at 0.01 steps in r-cmf is shown on both plots. Planets consistent with the r-cmf of Mercury and Earth shown with dashed-dotted and dotted lines. Earth and Ganymede shown on the ternary diagram.	111
6.2 1- and 2- σ mass and radius for Trappist-1 d-h from Agol et al. (2021). Four lines of constant interior structure are shown.	113
6.3 <i>Left</i> , interior structures which match 5000 draws of mass and radius for T1d. <i>Right</i> , interior structures for T1h. <i>Red lines</i> show the median and $\pm 1\sigma$ bounds of wmf across uniform r-cmf.	114
6.4 <i>Top</i> , the 1σ wmf of all 5 planets across r-cmf on a ternary. <i>Bottom</i> , same as top on a wmf vs r-cmf plot with 1σ shaded.	116
6.5 <i>Left</i> , the wmf at uniform r-cmf which match the observations of Grimm et al. (2018). <i>Right</i> , the wmf at uniform r-cmf which match the observations of Agol et al. (2021). <i>Red lines</i> show the median and $\pm 1\sigma$ bounds of wmf across uniform r cmf. <i>Right</i> , the wmf of Agol et al. (2021) at a given cmf and the $\pm 1\sigma$ compositions from Acuna et al. (2021).	117
6.6 Three likely structures of T1f visualized in Blender. In a.) the best-fit wmf for an Earth-like R-CMF with a Ice Ih surface (lightest blue). The planet still has layer of olivine (lightest green) and rwd (under olivine). In b.) the best-fit wmf for a Mercury-like R-CMF with ice X (darkest blue) layer above bridgmanite (medium green). In c.) the best-fit for no water with 14% cmf showing many mantle mate rials. Post-perovskite is shown in the darkest green.	117
6.7 The 1σ (<i>darker dashed</i>) and 2σ (<i>light dotted</i>) bounds and median in solid line of wmf with r-cmf for samples of gaussian mass and radius similar to that of T1f with varying mass uncertainty represented by the three colors.	119
6.8 <i>Left</i> , 1σ and 2σ ellipses of mass and radius for uncorrelated data (<i>red</i>), Agol et al. (2021) (<i>blue</i>), and highly correlated data (<i>cyan</i>). All distributions have the same median and standard deviation. <i>Right</i> , inferred wmf at given r-cmf for the three distributions from <i>left</i> with the shown correlation-coefficient.	120
6.9 <i>Top</i> , distributions of radius and density for my injected skewed distributions. <i>Bot tom</i> , likely wmf of the model data with various skewness. Skew-1, Skew-2, and Skew-3 correspond to the third, fourth, and fifth data set (row) in Table 6.2, and Skew-n is the negative skewed first sample.	121

6.10 Wmf with four large model differences. “Default” is our default model shown in Fig. 6.5. “water” raises the surface temperature to 300 K melting the layer of ice ih. “No-RWD” ignores upper-mantle materials removing the small layer of RWD. “Melt” has a 1500 K discontinuity at the mantle-hydrosphere boundary and core-mantle boundary which creates a liquid core layer. 123

xii

6.11 Wmf for the median values of mass and radius for T1f, but with varying values for experimentally determined EoSs. We vary parameters such as the bulk modulus but the uncertainty reported in the literature in 5000 draws. *Top*, uncertainty in our default EoSs. *Bottom*, uncertainty including uncertainty in the thermal conductivity of ice VII from Fei et al. (1993). 126

xiii
Chapter 1

Introduction

1.1 Small Exoplanet Demographics

There are currently 5312 confirmed planets in 3981 stellar systems outside of the Solar System¹. While 4011 of these exoplanets are transiting allowing us to measure their radii from the periodic decreases in the light curve of their star, exoplanet discovery and observing techniques are diverse including pulsar timing variations (Konacki & Wolszczan 2003), radial velocity (RV) (Butler et al. 2006), astrometry (Sahlmann et al. 2013), microlensing (Bennett et al. 2008), and direct imaging (Chauvin et al. 2004). “Hot Jupiters” with large sizes and short orbital periods, which most observational techniques are biased toward, were the first exoplanet category to be discovered Mayor & Queloz (1995). These extreme worlds of expanded hot gas showed that exoplanet systems may look wildly different from the Solar System.

Discoveries such as Kepler-10b, LHS 1140b, the seven planets of the Trappist-1 system, Ross 128b, and Proxima Centauri b (Batalha et al. 2011; Dittmann et al. 2017; Gillon et al. 2017; Bonfils et al. 2018; Anglada-Escudé et al. 2016) show that small exoplanets, less than ten Earth-masses, are now also firmly within observational capabilities. While they are difficult to observe, occurrence rates show that small planets between 1-4 R_{\oplus} , although not present in our solar system, are the most common type of planet in our galaxy (e.g. Batalha et al. 2013; Fressin et al. 2013; Pe

¹NASA Exoplanet Archive, <https://exoplanetarchive.ipac.caltech.edu/>, as of 20

igura et al. 2013). The search for planets with bulk properties similar to Earth is a focus

of many current and future space and ground based observatories such as the Transiting Exoplanet Survey Satellite (TESS) which has an expected 4000 planets yet to be confirmed (Huang et al. 2018), the PLATO (Planetary Transits and Oscillations of stars) mission which is scheduled to launch in 2026 (Heller et al. 2022), and the Extremely Large Telescope scheduled for completion in 2025 which is designed with the capabilities to image rocky planets (Udry et al. 2014).

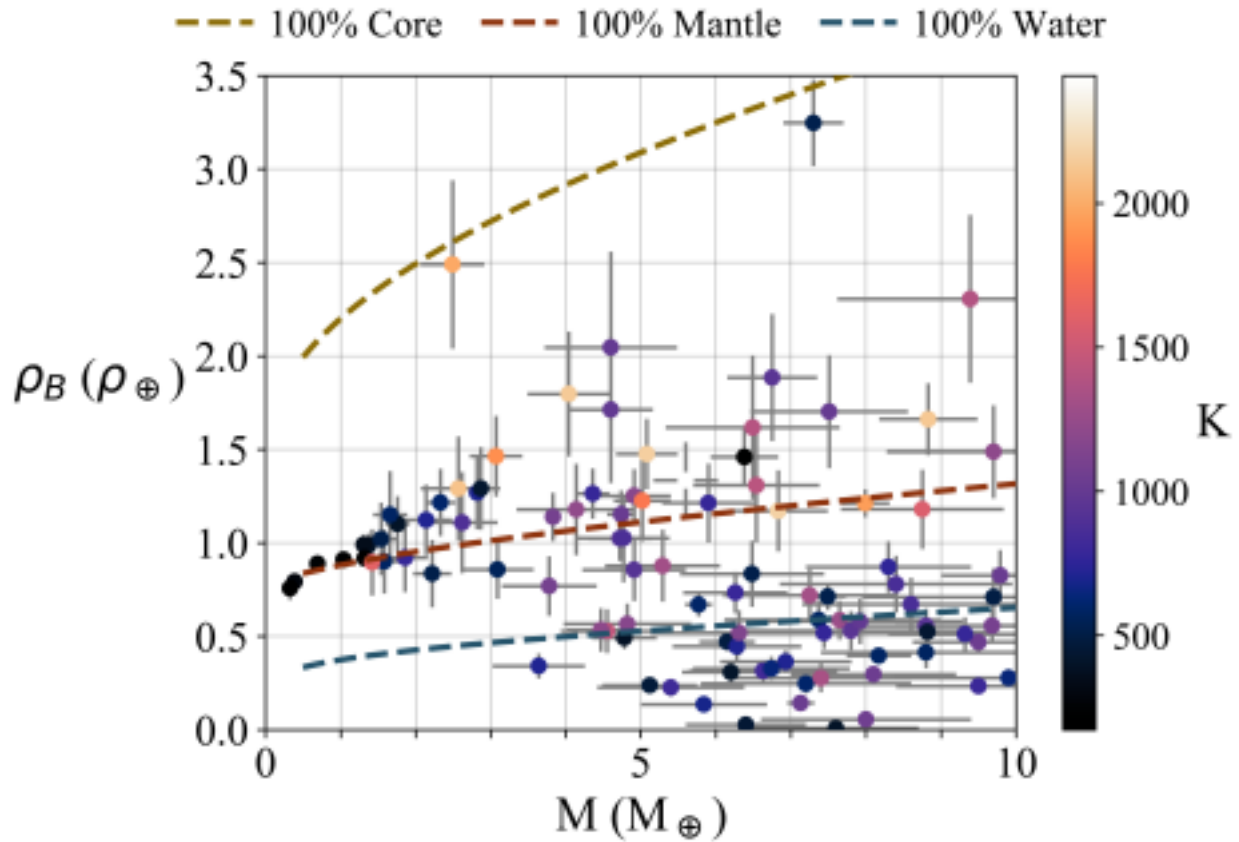


Figure 1.1: The bulk density with planet mass of confirmed exoplanets with both accurately determined mass and radius. Null-albedo equilibrium temperature of the planets are represented by color. Three lines of constant interior structure are shown for 100% core, 100% mantle, and 100% water planets.

The sample of confirmed planets gets smaller as we divide the parameter space. Only 2400 planets have a confirmed mass or projected planetary mass ($m \sin i$, measured by RV), and only 288 of those planets have masses less than ten times the mass of the Earth (defined as “small” in this work). Figure 1.1 shows the 98 confirmed planets with accurately determined radii and masses below 10 Earth-masses and with a null-albedo equilibrium temperatures below 2500 K². “Accurate” here refers to mass uncertainties less than 20% and radius uncertainties less than 10%. The melting temperature of olivine is approximately 1800 K. Equilibrium temperature is calculated

by

$$2a(1 - A_B)^{1/4} \quad (1.1)$$

$$T_{eq} = T_*$$

$$R_*$$

where T_* and R_* are the stellar temperature and radius, a is the semi-major axis, and A_B is the albedo which we take as 0. The null-albedo equilibrium temperature is a maximum temperature of the outer region of the planet. The bulk density

$$\rho_B = M/R^3 \quad (1.2)$$

is found from the planet’s mass, M , and radius, R , with uncertainties σ_M and σ_R . The uncertainty in density is thus given by propagation of error,

$$\sigma_{\rho_B} = \rho_B \left(\frac{\sigma_M}{M} + \frac{3\sigma_R}{R} \right), \quad (1.3)$$

if the mass and radius uncertainties are assumed independent. The planets are in 72

planetary systems. Mass and radius uncertainties are treated as symmetric, and we take an average of the

²NASA Exoplanet Archive, <https://exoplanetarchive.ipac.caltech.edu/>, as of 10

August 2022 3

upper and lower standard error if unsymmetrical. Density uncertainties are a maximum of 28%. This sample of planets show that exoplanets have bulk densities which range from dense and iron-rich (Santerne et al. 2018) to low density and volatile-rich (Leger et al. 2004). Although they are the most difficult to observe because they have the smallest radii, we see planets near the 100% core line in Fig. 1.1 and ones with various core mass fractions (cmf) between the 100% core and 100% mantle lines. Below the 100% mantle line, planets require greater volatile contents which may be in the form of a water-rich hydrosphere or below the 100% water line small planets require thick atmosphere envelopes. “Small” planets in this work thus encompasses classes of planets previously suggested like Mars-like, Earth-like, Super-Earth, mini-Neptune, sub-Neptune, water world, and super-Ganymede.

One of the most influential results in recent small exoplanet science is Fulton et al. (2017) which shows that the radii of 2025 small planets observed by *Kepler* form two distinct populations. The smaller planets are likely terrestrial-like and the larger are enriched in volatiles (e.g. Owen & Wu 2013; Rogers 2015; Ginzburg et al. 2016) with a low probability of planets having radii between 1.5 and 2 Earth-radii. The bi-modality is most commonly explained by planets forming with H/He dominated primary atmosphere envelopes which are either lost or held onto. The loss process could be dominated by photoevaporation (Lopez & Fortney 2013; Rogers et al. 2021) or core powered

mass-loss (Gupta & Schlichting 2019; 2020). Studying these two populations around various stellar types, various stellar ages, modeling their evolution, and quantifying the emptiness of the gap are active areas of study.

Investigations into these populations and identifying further categories of small exoplanets will require demographic studies of composition. However, the interior structure of a differentiated planet is degenerate with the bulk density as explored in

Rogers & Seager (2010). Mass-Radius 4

relationships, which describe the relationship of mass and radius for a given planet composition and interior structure, are useful when probing planet populations (e.g. Sotin et al. 2007; Weiss & Marcy 2014; Neil & Rogers 2020), but are not unique when considering differentiated planets of three or more layers. We must understand planet building materials and have accurate models for planet interiors to understand the small planet population.

1.2 Main Components of Small Planet Interiors

The Solar System has diverse small planetary bodies with only one that supports abundant life. This diversity extends beneath the surface of the terrestrial planets. Mercury's core makes up 70-80% of its mass (Hauck et al. 2013) compared to the 33% cmf of the Earth. Icy moons, like Ganymede, hold upwards of 45% of their mass in a water-ice hydrosphere (Kuskov & Kronrod 2005). Above the surface, Venus's atmosphere is ~0.01% of its mass making the surface pressure 90 times that of Earth. These differences in structure are tied to important aspects of habitability such as volatile abundance, cooling history, chemical cycling, and the generation of a magnetic

field (Astro2020 white papers: Pontoppidan et al. 2019; Apai et al. 2019; Lazio et al. 2019; Hu et al. 2019).

We have little information on the interiors of planetary bodies as the deepest hole ever dug, Kola Superdeep Borehole, made it to a depth only 0.2% of the Earth's radius (Kozlovsky 1982). Most of our knowledge on interiors comes from seismology which we have abundant observations of on Earth (Romanowicz 2008). *InSight* also gathered limited seismic data on the interior of Mars (Khan et al. 2021; Knapmeyer-Endrun et al. 2021; Stahler et al. 2021). Satellites, such as MESSENGER, Cassini, and Juno, gather important data on the gravitational moment of plan

5

ets and moons which constrains the interior structure (Helled & Fortney 2020). BepiColumbo and a future Uranus probe will be important to better understanding Mercury and Uranus's interior structure. From meteorites, we know the primordial composition in the Solar System from calcium-aluminum rich inclusions, and we know that even small bodies differentiate into layers of distinctive density (McSween Jr & Huss 2022). Vesta in the asteroid belt is 20,000 times smaller than the Earth but it and similar bodies are the progenitor of the differentiated (achondritic) HED meteorites (McSween Jr et al. 2013). Because of our limited data, many of our assumptions on interiors is Earth-centric. In this section, I review a few important aspects of major differentiated layers.

1.2.1 Cores

Iron and nickel are two orders of magnitude more abundant in the Solar System than elements of higher atomic number. As major rock forming elements with high density, iron differentiates early in planetary bodies as it rains from molten mantles releasing gravitational energy as heat as it forms an iron core. The heat from core formation creates somewhere between a 500-1800 K temperature discontinuity between the hot core and mantle (Nomura et al. 2014; Lay et al. 2008). The iron and nickel alloy with estimates ranging from 5-20% nickel for the Earth (Hirose et al. 2021). The nickel content of iron meteorites is measured in Benedix et al. (2000).

Planetary cores are at extreme heat and pressure. The Earth's central pressure is over 350 GPa and temperature is over 5500 K similar to the temperature of the sun's photosphere. A planet ten times the mass of the Earth reaches 6 TPa in the center near 10 times the highest pressures reached in the laboratory. At these pressures iron takes a hexagonal close-packed (HCP) structure. The

6

HCP arrangement has the highest packing efficiency of sphere along with face-centered cubic at 74%.

The core of Earth is inferred to be 5-10% less dense than pure iron, also known as the "density deficiency" (Hirose et al. 2013). The core has some mix of unknown lighter elements such as silicon, oxygen, sulfur, carbon, and hydrogen. These lighter elements affect the crystalline phases, physical properties, and melting temperature of the core. Mars's core may be entirely liquid which is most likely a result of sulfur decreasing the melting temperature (Stahler et al. 2021). "

1.2.2 Mantles

The mantle of the Earth holds diverse silicates made with lithophile elements. The upper mantle is 60% olivine, $(\text{Mg}, \text{Fe})_2\text{SiO}_4$, by volume. The other 40% varies by depth in proportion of garnet to pyroxene in the clinopyroxene to orthopyroxene crystalline structure. These minerals hold the aluminum and calcium in the mantle. The major orthopyroxene mineral is enstatite, MgSiO_3 . At pressures above 15 GPa the olivine changes to wadsleyite with an orthorhombic structure and at above 20 GPa to ringwoodite in a spinel structure. At this pressure, in the uppermost parts of the lower mantle, the other major mineral becomes majorite (majoritic garnet, MgSiO_3) which forms solid solutions with Al, Fe, and Ca-bearing garnets.

The upper (and upper-lower mantle) is complex, but as pressures reach 25 GPa at depths over 650 km the main mineral becomes bridgmanite, $(\text{Mg}, \text{Fe})\text{SiO}_3$. While periclase/magnesiowustite " " is about 10% of the lower mantle by volume, bridgmanite is over 80% by volume. Hence, over 40% of the Earth's entire mass is in bridgmanite. Deep in the Earth's mantle above 100 GPa the bridgmanite takes another crystalline form referred to as post-perovskite. Although post-perovskite

7

layer is small in the Earth it influences thermal transport in the D" layer above the core-mantle boundary, and would be a major component of mantles for larger planets. See Kaminsky (2012) for a review of these topics.

The mantles of exoplanets may have large differences in the Ca, Al, Mg, and Fe

abundances changing the dominate mineralogy Unterborn et al. (2023). However, less Earth-like mantles may be possible in other systems. Carbon planets are proposed to have mantles that are composed of SiC, graphite and diamond, or even carbonates in rare situations Kuchner & Seager (2005); Seager et al. (2007); Unterborn et al. (2014). Mantles may also hold large amounts of water and other volatiles; possibly enough to change the bulk properties of the rock (Dorn & Lichtenberg 2021)

1.2.3 Volatile Layers

Water is the most abundant volatile in the Solar System after hydrogen and helium. Thus past the ice-line planetary bodies are formed from water rich materials and have water mass fractions over 50%. While the water storage of the mantle is an active area of research, water's low density leads it to forming a hydrosphere on the planet's surface. Earth's hydrosphere is only 0.023% of Earth's mass.

A planet with a large hydrosphere will reach pressures which forces the water to the solid phase at depths as low as 80 km (comparable to depth of Earth's lithosphere). H₂O's polar nature leads to a complex phase diagram with at least 18 known phases. While hexagonal ice, Ice Ih, is the kind we experience at standard pressure and cold temperatures, at high pressure pressure water transforms to tetragonal Ice VI and cubic Ice VII. At a debated pressure between 30 and 120 GPa Ice VII transitions from a double well potential to a single well potential. This Ice X is 2 times

2021). Grande et al. (2022) describes a transitional tetragonal phase Ice VII_t between Ice VII and Ice X. While I do not consider this assumption in this work, little work has been done on non-pure water in exoplanet systems. Since water is a powerful solvent, a planet's hydrosphere may have different properties from the common pure water assumption.

In this work, I focus primarily on planets with no or small secondary atmospheres. However, atmospheres are essential to understanding the entire population of planets less than 10 Earth masses. Many concluding sections of chapters (Sec. 3.4, 4.6) discuss future work on combining interiors and atmospheres.

1.3 Planet Interior Solvers

Solving the interior of a planet brings together multiple disciplines from geology to high pressure material physics to planetary science. Interior models were first used for exoplanets in Leger et al. (2004), Valencia et al. (2006), Sotin et al. (2007), and Seager et al. (2007). These ' models are one dimensional modelling the planet as spherically symmetric. Inside of the planet the equations of hydrostatic equilibrium must be satisfied—the pressure must be continuous and the gradient increasing inside of the planet balanced by the gravitational force acting on the planet.

With an interior structure model the pressure, density, temperature, and radius can be found as a function of enclosed mass. Boundary conditions are a radius of zero at an enclosed mass of zero and a surface temperature and pressure. Models generally assume that the planet is fully differentiated into distinct compositional shells. With a shell model, each layer can be solved with a different material. The equation of state

(EoS) of each material describes the volume at pressure

9

and temperature conditions.

Planets are generally assumed to follow isentropic temperature gradients. This temperature gradient assumes that heat transfer occurs only through conduction, without any convective heat transfer or energy being added or removed from the system. This approximation is reasonable for large, old, slowly cooling planets. With an isentropic temperature profile, temperature changes with depth due to changes in pressure and density following the adiabat based on material properties. An isentropic temperature gradient with discontinuities at boundary layers match the seismic data from Earth (Stacey & Davis 2008).

Underlying the many different models used for exoplanet interiors are various computational techniques (e.g. shooting Nixon & Madhusudhan (2021) or relaxation Unterborn et al. (2018)) and treatments of temperature (e.g. isothermal Seager et al. (2007) or isentropic Hakim et al. (2018)). Most importantly, these models must choose for each material an EoS. These choices often differ between studies.

In Fig. 1.2, I show the works that inform two recent interior studies. The two studies each exemplify a theme of this thesis: improving interior models and characterizing exoplanets. Dorn & Lichtenberg (2021) explores the storage of water in hot planets. Acuna et al. (2021) characterizes ~ the interiors of the Trappist-1 planets. These two studies are built upon different legacies of interior codes with some model parameters not cited in the top-level publication. Take for example the ice phases which are based

on Bezacier et al. (2014) in Acuna et al. (2021) and Wagner & Pruß (2002) ~ in Dorn et al. (2015). Acuna et al. (2021) relies on EOS from the 1990s in both the mantle and ~ core. In addition, both of these models are not open-source.

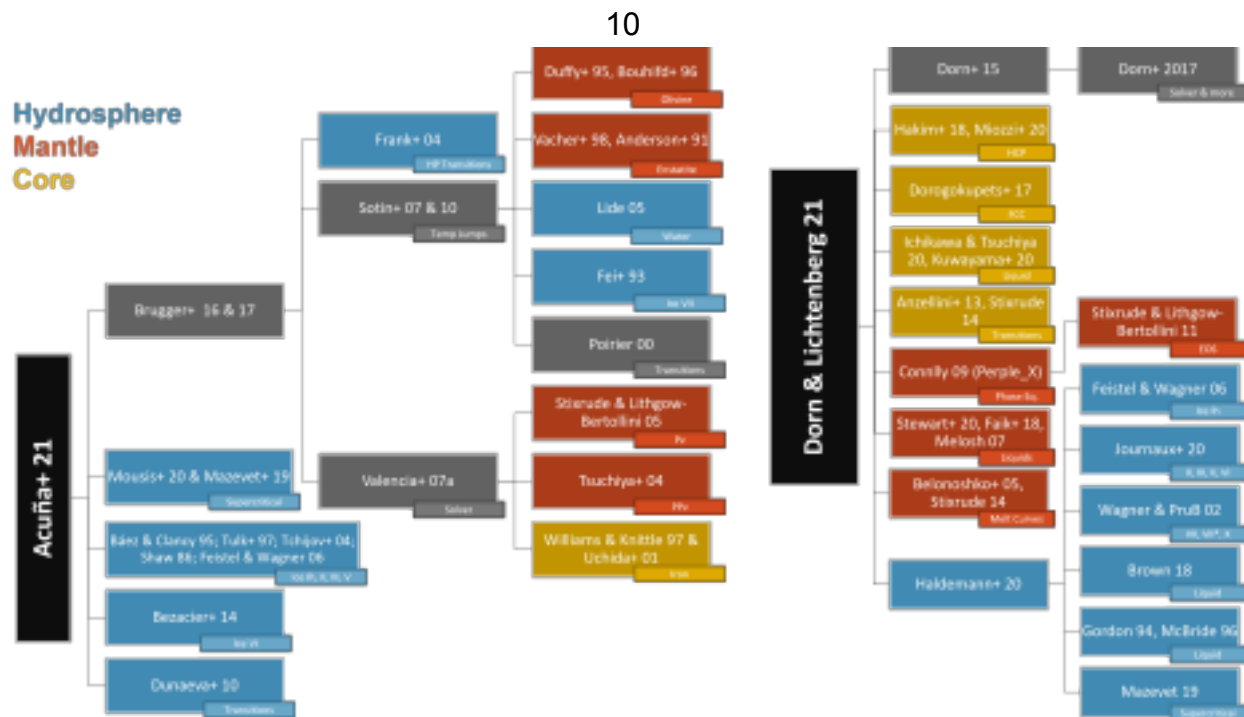


Figure 1.2: The works that inform the planet interior model in two recent planet interior works— Acuna et al. (2021) and Dorn & Lichtenberg (2021). Tree structure shows previous works the models are built upon which are not all cited in the top-level paper. Works color coded by layer they inform. Works in figure: Bragger et al. (2016; 2017); Sotin et al. (2007); Valencia et al. (2007b); Frank et al. (2004); Duffy et al. (1995); Bouhifd et al. (1996); Vacher et al. (1998); Anderson et al. (1991); Lide (2002); Fei et al. (1993); Poirier (2000); Stixrude & Lithgow-Bertoloni (2005); Tsuchiya et al. (2004); Williams & Knittle (1997); Uchida et al. (2001); Mousis et al. (2020); Mazevet et al. (2019); Baez & Clancy (1995); Tulk et al. (1997); Tchijov (2004); Shaw (1986); Feistel & Wagner (2006); Bezacier et al. (2014); Dunaeva et al. (2010); Dorn et al. (2015; 2017b); Hakim et al. (2018); Miozzi et al. (2020); Dorogokupets et al. (2017); Ichikawa & Tsuchiya (2020); Kuwayama et al. (2020); Anzellini et al. (2013); Stixrude (2014); Connolly (2009); Stewart et al. (2020); Faik et al. (2018); Melosh (2007); Belonoshko et al. (2005a); Stixrude (2014; 2012); Haldemann et al. (2020); Journaux et al. (2020); Wagner & Pruß (2002); Brown (2018); Gordon & McBride (1994); McBride & Gordon (1996); Mazevet et al. (2019).

1.3.1 Applications to Small Planets

There are numerous works built upon interior models for small planets. Demographic-focus studies focus on the mass-radius relationship and describing compositions of planet populations. Zeng et al. (2016) develops semi-empirical mass-radius relations for two-layer rocky planets enabling quick approximations. Suissa et al. (2018) give the minimum and maximum core mass fraction an observed planet may have. Neil & Rogers (2020) develop a broken power-law relationship which match the mass-radius measurements of *Kepler* planets. They find the planets are best fit by a mixture model which considers gaseous envelope, evaporated core, and intrinsically rocky planets.

A number of studies tie other observable properties than mass and radius to planet interiors. Stellar composition may be used as a constraint on interiors. Scora et al. (2020), Schulze et al. (2021a), and Bonsor et al. (2021) explore this possibility from formation and observations and find evidence that most planets reflect their stars elemental abundances, although they may need to be devolatilized (Wang et al. 2019). Putirka & Xu (2021) investigate mantle material in white dwarf pollution finding non-Earth like mineralogy and Buchan et al. (2022) shows Ni and Cr in pollution can be used to constrain the core mass of the polluting body. As a last example, Price & Rogers

(2020) constrain the cmf that an ellipsoid planet stretched by its close in orbit must have to stay intact.

Several sub-fields are building upon interior studies. Zhang & Rogers (2023) focuses on liquid layers in planets and explores the thermal evolution of planets from their formation. O'Neill & Lenardic (2007) and Meier et al. (2021) investigate planet convection. VPLANET (Barnes et al. 2020) compiles and couples a number of models related to habitability including a module for

12

interior thermal evolution with a focus on magnetic fields and plate tectonics. Works on planet collisions like Marcus et al. (2009; 2010) and Lock & Stewart (2017) involve using interior models to inform smoothed-particle hydrodynamics simulations. As a final example, a large body of work is concerned with coupling thick sub-Neptune atmospheres to interiors starting with Fortney et al. (2007) and including Howe & Burrows (2015) and Chen & Rogers (2016).

1.4 Overview

To determine if small exoplanets exhibit as diverse interior structures as the Solar System, we need robust and reproducible community standards for interior modeling. Communicating results from geology and material physics to the astronomy community and visa versa must be a priority. We must understand how model choices and uncertainty are affecting our inferences of planet composition.

In this work, I develop an open-source interior model with flexible model parameters,

Chapter 2. I further its abilities to characterize observed planets, Chapter 3, and improve several aspects of our model, Chapter 4. I then turn to characterizing observed planets in a number of collaborative works, Chapter 5. This improved model and my understanding of planet characterizations culminates in a study which quantifies the uncertainties in our planet inferences for small planets from observation, model, and experimental uncertainties, Chapter 6. Throughout this work, I reiterate this introduction, give background on important concepts in exoplanets and planet interiors, and connect my work with the expansive literature on exoplanets. I summarize the work in Chapter 7.

13 Chapter 2

MAGRATHEA: an Open-Source Spherical Symmetric Planet Interior Structure Code

2.1 Background

As explored in Chapter 1, the community uses a variety of models to characterize the interior structure of planets. Underlying these models are differing computational techniques (e.g. shooting in Nixon & Madhusudhan (2021), relaxation in Unterborn et al. (2018), or calculus of variation in Zeng et al. (2021)) and numerous experimental measurements and theoretical estimates of the equation of state (EoS) for planet-building materials. For example, a number of models use bridgmanite primarily in the mantle and do not include high-pressure post-perovskite (Grasset et al. 2009;

Zeng et al. 2016; Brugger et al. 2017; Michel et al. 2020) while others capture detailed upper-mantle chemistry (Valencia et al. 2007b; Dorn et al. 2017b; Unterborn & Panero 2019) and recent work adds liquid silicates (Noack & Lasbleis 2020). Another point of difference is the model's temperature profile with some using an isothermal mantle (Seager et al. 2007) rather than isentropic (Hakim et al. 2018). While others limit isothermal modeling to the water layer (Sotin et al. 2007; Brugger et al. 2016) and the atmosphere (Madhusudhan et al. 2021; Baumeister et al. 2020). Newer models try to capture the complex phase diagram of water (Mousis et al. 2020; Journaux et al. 2020; Haldemann et al. 2020), the hydration of mantle materials (Shah et al. 2021; Dorn & Lichtenberg 2021), and couple the atmosphere to the interior (Madhusudhan et al. 2020; Acuna et al. 2021). ~

14

In Huang et al. (2022), collaborators (Dr. Chenliang Huang and Dr. Jason Steffen) and I (second author) document the development of MAGRATHEA¹ an open-source planet interior solver that can be customized to different user-defined planet models. Compared to other codes, the package is designed to enhance ease-of-use and flexibility. MAGRATHEA features phase diagram options and transparent EoS formatting, which enables the user to choose between a large library of EoSs (equations of state) and add/change materials and equations.

We are motivated by our collaboration with high-pressure physicists to understand how uncertainties in experimental EoSs affect predictions of planet interiors. In Huang et al. (2021), also reported in Sec. 4.2, we use our adaptable planet interior model to implement new measurements for high-pressure water-ice from Grande et al. (2022).

Their experiments confirmed the pressure of the transition from ice-VII to ice-X and identified a transitional tetragonal ice-VII_t phase. This improved H₂O equation of state changed the predicted radius of a pure water, 10 M_⊕ planet by over four per cent from Zeng et al. (2016).

In this chapter, we document the features and demonstrate the functionality of MAGRATHEA. The most up-to-date version is hosted on the GitHub platform. This chapter is laid out as follows. We describe the fundamentals of a planet interior solver in Section 2.2. In Section 2.3, we describe the specifics of our code and how to build a planet model within the code. A model is designated by defining a phase diagram for each layer and choosing an equations of state from our library for each phase. We discuss limitations to our default model in 2.4. We describe the code's functionality and discuss various tests in Section 2.5. We demonstrate the EoS storage and functionality in Section 2.6 and 2.7 and end with some summarizing remarks in Section 2.8.

¹Magrathea is the legendary planet where hyperspatial engineers manufacture custom-made planets in Douglas Adams's *The Hitchhiker's Guide to the Galaxy* (Adams 1995-2001).

15

2.2 Interior Structure Solver

We consider a simplified planet structure with four layers: an iron core, a silicate-dominated mantle, a hydrosphere of water/ice, and an ideal gas atmosphere. We assume these layers are spherically symmetric and that a single solution to composition at a given pressure and temperature exists within each layer. Our approach is similar to other interior structure solvers used for exoplanets (e.g. Leger et al. 2004; Valencia et al. 2006; Sotin et al. 2007; Seager et al. 2007). A schematic depiction of MAGRATHEA from

input to output is shown in Fig. 2.1. Given the mass of each of these layers, $M_{\text{comp}} = \{M_{\text{core}}, M_{\text{mantle}}, M_{\text{hydro}}, M_{\text{atm}}\}$, the code calculates the radius returning the pressure $P(m)$, density $\rho(m)$, and temperature $T(m)$ with enclosed mass m by solving the following four equations:

1. Mass continuity equation

$$\frac{dm}{dr(m)} = 4\pi r^2 \rho(m), \quad (2.1)$$

2. Hydrostatic equilibrium

$$\frac{dm}{dP(m)} = -\frac{Gm}{4\pi r^4}, \quad (2.2)$$

3. Temperature gradient

If the isothermal option is chosen, the temperature gradient is 0. When the isentropic option is chosen, depending on the available thermal properties of the phases, the temperature gradient can be calculated using either of the following two formulae. If the Gruneisen parameter "

γ is available,
we can have $dm = dT$

$$s dV d\rho$$

$$\frac{d\rho}{dm}$$

$dT(m)$

$$dV$$

$$= \frac{\rho^2}{dT dV} \frac{\partial \rho}{\partial P} \frac{dm}{\rho} \frac{dP}{\partial T} \frac{dT dm}{\partial T} \cdot$$

$dT(m)$

$$\frac{dT dV}{\rho^2}$$

Thus,

$$\frac{dT}{\rho}, (2.3)$$

where

$$dm = \frac{\rho^2}{m_{\text{mol}} \frac{\partial \rho}{\partial P} \frac{\partial \rho}{\partial T}}$$

$$= \frac{dT}{T} \frac{dV}{\rho^2} \frac{\partial \rho}{\partial P} \frac{\partial \rho}{\partial T}$$

$$s = - \frac{\gamma T}{V}, (2.4)$$

$$dT dV$$

m_{mol} and V are the molar mass and volume respectively.

Alternatively, if the thermal expansion α is available, we can have

$dT(m)$

$$dm = - \alpha T G m$$

$$4 \pi r^4 \rho c_p, (2.5)$$

where c_p is the specific heat capacity at constant pressure.

4. Equation of state (EoS)

$$P(m) = P(\rho(m), T(m)), (2.6)$$

which is unique for each material/phase.

The boundary conditions of the model are $r = 0$ at $m = 0$ and the user-defined surface temperature and pressure, $T(M_p)$ and $P(M_p)$. The default surface pressure is 100 mbar approximately the pressure level of the broad-band optical transit radius probes (Grimm et al. 2018). Since a rapid

17

temperature jump may occur at the boundary between chemically distinct layers, where heat can only transfer conductively (Valencia et al. 2006), the user can also set a temperature discontinuity, T_{gap} , at the boundary of adjacent layers. The Earth is often modeled with a discontinuity ranging from a 300 to 1100 K increase across the core mantle boundary (Nomura et al. 2014; Lay et al. 2008) and (Valencia et al. 2007b) and (Sotin et al. 2007) use discontinuities in their exoplanet models. In our demonstrations in Section 2.5, we use planets that are in thermal equilibrium between their layers with $T_{\text{gap}} = \{0, 0, 0, T(M_p)\}$.

The user can choose between isothermal and isentropic temperature mode by adjusting an *isothermal* flag of the integrator. When the flag is set to true, the whole planet is assumed to be isothermal (except the atmosphere layer, see section 2.3.8). When the input EoS parameters of a phase are not sufficient to calculate the isentropic temperature gradient (see section 2.2.2), this specific phase would be treated as isothermal, regardless of the value of the *isothermal* flag.

2.2.1 Phase Diagrams

We model our planets with distinct differentiated layers with defined mass fractions. However, within each layer the phase may change due to the large pressure and temperature ranges. When integrating within a layer, the code first checks the pressure and temperature to determine the appropriate region of the phase diagram. A built-in phase function outputs a link to the EoS of the material or phase in the region. The density ρ or the volume of unit cell V can then be solved from the EoS (Eq. 2.6).

A key feature of MAGRATHEA is the user's ability to change the phase diagram in each layer and choose between EoSs for each phase. Fig. 2.2 shows our default phase diagram and Sec. 2.3.3

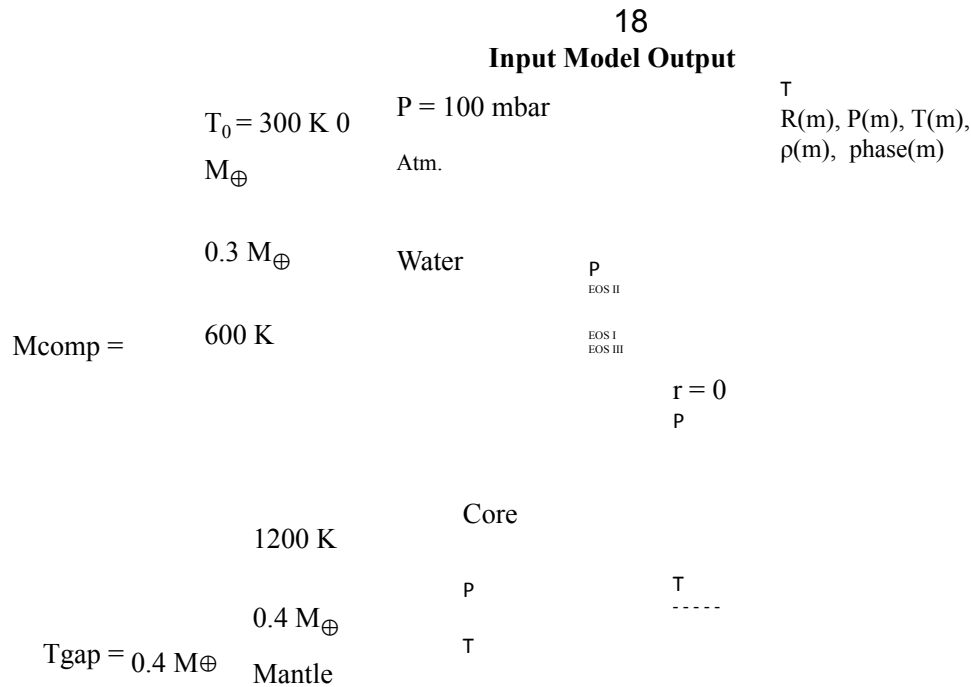


Figure 2.1: A schematic overview of MAGRATHEA. Showing an example input, *left*, of a $1.1 M_\oplus$ planet with $0.4 M_\oplus$ core, $0.4 M_\oplus$ mantle, and $0.3 M_\oplus$ hydrosphere. The planet is not in thermal equilibrium with a surface temperature of 300 K and jumps in temperature across boundary layers of 600 K and 1200 K. *Center*, shows MAGRATHEA's four input

layers with cartoons of phase diagrams defined for each layer with an EoS chosen for each phase. Default phase diagrams shown in Fig. 2.2. *Right*, shows the pressure and temperature with enclosed mass. The radius at boundaries and the planet radii is also shown.

19

further details their implementation. The atmosphere layer is not shown in the plots and has two “phases”, isothermal for $P < 100$ bar and adiabatic for $P > 100$ bar.

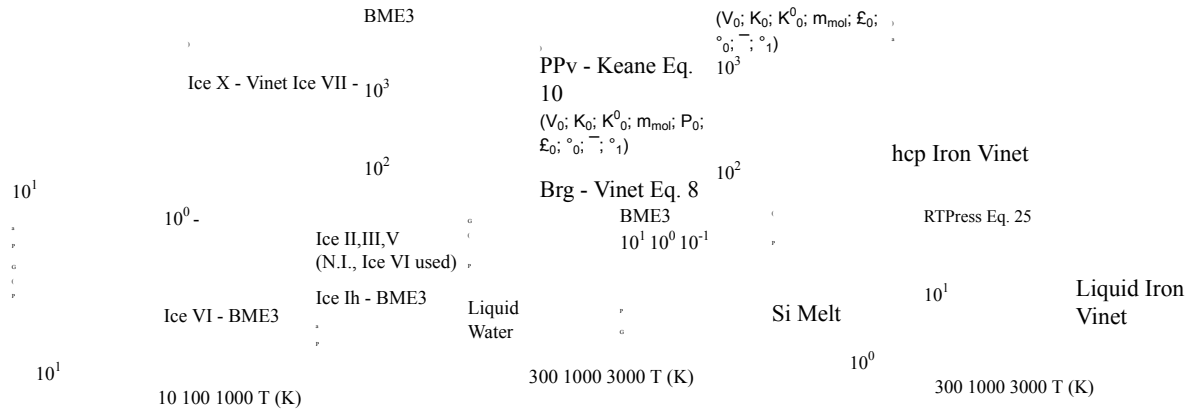


Figure 2.2: Default phase diagrams for hydrosphere, mantle, and core layers. EoS and phase transitions from a variety of sources detailed in Sec. 2.3.4. Type of EoS fitting equation shown from Sec. 2.2.2. Additionally, the parameters for mantle EoSs are shown, *middle*. The phase diagrams and choice of EoS can be customized by the user. *N.I.* is *not implemented*. The atmosphere layer also has a phase function, but our default is ideal gas at all pressure and temperatures, see Sec. 2.3.8

2.2.2 Equation of State Formulae

The density of a phase at certain temperature and pressure is determined by the

EoS, which can be fed into MAGRATHEA either through an analytical fitting formula or a tabulated pressure density table. For the first option, each material's EoS must provide the parameters for one of the following formulations.

According to the Mie-Gruneisen-Debye (MGD) formulation, the total pressure P can be divided into an isothermal term P_c , and a thermal term, P_{th} , expressed as (Dewaele et al. 2006):

$$P(V, T) = P_c(V) + P_{th}(V, T) - P_{th}(V, T_0) \quad (2.7)$$

20

MAGRATHEA includes four common types of the EoS that give the reference isotherm P_c , including:

1. The Eulerian finite strain Birch-Murnaghan EoS (BME) is the most commonly used EoS. The fourth-order BME (Seager et al. 2007) is

$$P_c = \frac{3}{2} K_0 \eta^{7/3} - \eta^{5/3} \quad (2.8)$$

$$1 + \zeta_1(1 - \eta^{2/3}) + \zeta_2(1 - \eta^{2/3})^2,$$

where

$$\eta = V_0/V, \quad \zeta_1 = \frac{3}{4}(4 - K'_0)$$

$$\zeta_2 = \frac{3}{8} K_0 K''_0 + K'_0(K'_0 - 7) + \frac{143}{9}.$$

$K = -V (\partial P / \partial V)_T$ is the isothermal bulk modulus, K' is the first derivative of the bulk modulus with respect to pressure, and K'' is the second of the bulk modulus with

respect to pressure. The subscript 0 refers to quantities at ambient-pressure conditions. If ζ_2 is set to zero the EoS reduces to third-order BME.

2. Vinet EoS (Seager et al. 2007; Smith et al. 2018; Wicks et al. 2018), which is considered to give more accurate result than BME at high pressure or large compression (Poirier 2000)

$$P_c = 3K_0 \eta^{2/3} (1 - \eta)^{-1/3} \quad (2.9)$$

3

exp

$$2(K'_0 - 1) (1 - \eta)^{-1/3} ; 21$$

3. Holzapfel EoS (Bouchet et al. 2013)

$$x = (V/V_0)^{1/3} \quad (2.10)$$

$$c_0 = - \ln \frac{1003.6 \text{ GPa cm}^5}{3K_0 \text{ mol}^{-5/3} (Z/V_0)^{5/3}}$$

$$c_2 = \frac{3}{2} (K'_0 - 3) - c_0$$

$$P_c = 3K_0 x^{-5} (1 - x)$$

$$\exp (c_0(1 - x)) (1 + c_2 x(1 - x)) ;$$

4. Keane EoS (Sakai et al. 2016)

$$y = V_0/V \quad (2.11)$$

$$K'_\infty = 2 \quad Y_\infty + \frac{1}{6}$$

$$P_c = K'_0 K_0 K_\infty^2 y^{K'_\infty - 1} - (K'_0 - K'_\infty) K_0$$

$$K'_{\infty} \ln(y)$$

5. An empty placeholder is available for an additional formulation of the EoS such as from Choukroun & Grasset (2007).

For phases that only exist at high pressure, the bulk modulus, K_P , can be measured more precisely at the phase transition pressure, P_0 , than at ambient pressure (Salamat et al. 2013). If K_P is applied instead of K_0 , a constant pressure P_0 under which the bulk modulus is measured is added to the isotherm pressure. If the parameters to calculate the thermal term, P_{th} , are not provided, only P_c is calculated and a constant temperature is returned.

P_{th} is most commonly calculated from a quasi-harmonic Debye thermal pressure and

the an 22

harmonic and electronic thermal pressure, which are obtained from (Belonoshko et al. 2008; Duffy

et al. 2015)

$$P_{th}(T) = \frac{1}{V} E_{th}(T) + 3nR \quad 2Ve_0 x^g g T^2, \quad (2.12)$$

where

$$x = V/V_0 = \eta^3, \quad \gamma = \gamma_{\infty} + (\gamma_0 - \gamma_{\infty})x^{\beta} \quad (2.13)$$

$$\Theta = \Theta_0 x^{-\gamma_{\infty}} \exp \left(\frac{\gamma_0 - \gamma_{\infty}}{\beta(1 - x^{\beta})} \right) \quad (2.14)$$

$$z = \Theta/T, \quad E_{th} = 3nRT D_3(z). \quad (2.15)$$

D_3 indicates a third-order Debye function. Θ_0 , γ_∞ , γ_0 , β , e_0 , and g are fitting parameters, R is the gas constant, and n is the number of atoms in the chemical formula of the compound. A numerical

derivative of Eq. 2.7 γ_T and $\frac{\partial P}{\partial T}$ that are required in gives the $\frac{\partial P}{\partial \rho}$ the Eq. 2.3.

A different framework for the thermal term, referred to as RTpress in the following, is used in Wolf & Bower (2018) and built upon the Rosenfeld-Trazona model. In addition to the Gruneisen γ parameters, it has additional fitting terms with derivation in Wolf & Bower (2018). In RTpress, the Gruneisen parameter can be written as

$$\gamma = \gamma_{0S} \frac{C_V(V, T) + V b'(V)}{C_V(V, T_{0S}) b(V)} \Delta S^{\text{pot}}(T_{0S} \rightarrow T) \quad (2.16)$$

The subscript 0S stands for the quantity evaluated along the reference adiabat,

$$T = T_{0S} = T_0 \quad 1 + a_1 f + \frac{1}{2} a_2 f^2, \quad (2.17)$$

with,

$$f \equiv f(V) = \frac{V - V_0}{V_0} \quad (2.18)$$

$$a_1 = 6\gamma_0, \text{ and } a_2 = -12\gamma_0 + 36\gamma_0' - 18\gamma_0'', \quad (2.19)$$

where γ_0 is the Gruneisen parameter at zero GPa and $\gamma_0' = V_0(d\gamma/dV)_0$.

The Gruneisen parameter variation along the reference adiabat is "

$$\gamma_{0S} = (2f + 1)(a_1 + a_2 f) \quad (2.20)$$

$$b(V) = \sum_{n=0}^n b_n \left(\frac{V}{V_0} \right)^n \quad (2.21)$$

and

$$b'_n(V) = \sum_{n=1}^n b_n \frac{V^{n-1}}{V_0^{n-1}} \quad (2.22)$$

are a polynomial representation of the thermal coefficients and its volume derivative in cgs units.

The total heat capacity

$$C_V(V, T) = b(V) f^{(1)} \left(\frac{T}{T_0} \right) + \frac{3}{2} n R \quad (2.23)$$

is the sum of potential and kinetic contributions², where

$$f_T = \frac{T}{T_0} \quad (2.24)$$

$$\beta_T = \frac{\beta}{T_0} \quad \beta = \frac{1}{k_B T} \quad \beta - 1 = \frac{1}{k_B T_0} - \frac{1}{k_B T} \quad \text{To be consistent}$$

²We believe that Eq. B.3 in Wolf & Bower (2018) should read C^{kin} with the unit eV/atom chosen for b_n in their work, the number of atoms per formula unit should not be a factor.

24

The difference in entropy from the reference adiabat from the potential contribution is

$$\Delta S^{\text{pot}}(T_{0S} \rightarrow T) = b(V) \left(\frac{T}{T_0} \right)^{\beta-1} - b(V) \left(\frac{T_{0S}}{T_0} \right)^{\beta-1} \quad (2.25)$$

Finally, the thermal term of the pressure in the framework of Wolf & Bower (2018) can be written as

$$P_{th} = -b'(V) \frac{f_T}{T} + \gamma_{0S}(V) C_{V,0S}(V) \cdot (T - T_0) + \frac{b'(V)}{\beta - 1} \frac{f^{(1)}}{T - f^{(1)}} \frac{\tau(T_{0S})}{V} - T_0 \frac{\tau(T_0) - f^{(1)}}{\tau(T_{0S})} \quad (2.26)$$

Besides the MGD representation, the P-V-T equation of state can also be expressed as (Fei et al. 1993)

$$V(P, T) = V(P, T_0) \exp \left[\int_{T_0}^T \alpha(P, T') dT' \right], \quad (2.27)$$

$\alpha(P, T)$ is the thermal expansion, which has the form of

$$\alpha(P, T) = \alpha(T) \left[1 + K'_0 K_0 P \right]^{-\xi} \quad (2.28)$$

$\alpha(T)$ is the zero-pressure thermal expansion coefficient. For $T > T_0$, it is expressed as a linear function of temperature

$$\alpha(T) = \alpha_0 + \alpha_1 T. \quad (2.29)$$

For phases that adopt the thermal expansion representation, the Eq. 2.5 can be used

to calculate 25

adiabatic temperature gradient. The heat capacity in the equation can be calculated using the fitting formula

$$c_p = c_{p0} + c_{p1}T - c_{p2}T^2. \quad (2.30)$$

2.2.3 Tabulated Equation of State

In place of a fitting equation, the EoS can take the form of a tabulated density-pressure table which then code then interpolates. For MAGRATHEA the input file should have two columns, the first column is the density in g cm^{-3} and the second column is the pressure in GPa. The pressure must be strictly ordered. The first row of the table file, which contains header information, is skipped when the file is parsed. The program interpolates the table monotonically using the Steffen spline (Steffen 1990; no relation to our co-author) from the *gs/* package (Galassi et al. 2009).

2.2.4 User-Defined Function

For further flexibility, users can create or modify the EoS of a phase using their own C++ functions. MAGRATHEA supports three types of user-defined functions. First, a user can provide an EoS function that returns the material density as a function of pressure and temperature. In addition, either a temperature gradient, dT/dP , as a function of pressure and temperature or an entropy function dependent on density and temperature can be used to set up the temperature solver in a phase. If a user-defined temperature gradient function is set up, the temperature profile of this phase is not restricted to

isentropic. The density function and the temperature function (dT/dP or entropy) can also be used in combination for a phase. The method to import these user-defined functions is shown in Appendix 2.7.

2.3 Overview of the Code Structure

MAGRATHEA is written in C++ and relies on the *GNU Scientific Library (GSL)*³(Galassi et al. 2009). A step by step guide to run the code can be found in the *README* file on our GitHub repository.

The code is compiled with the included *Makefile*. The central interaction with the user occurs through *main.cpp*. The user may choose between seven modes by setting *input mode*. They include the regular solver, a temperature-free solver, a two-layer solver (Sec. 2.3.2), three methods to change the EoS during run-time (Sec. 2.5.3), and a bulk input mode for solving many planets with the regular solver in a single run (Sec. 2.5.4). Each mode requires the user to define the mass of each layer in the planet. In modes where the regular solver is used, the user defines a temperature array which gives the temperature at the surface and any discontinuities between layers. This section covers the specific design of the code and options that the user may choose between—the solver in Sect. 2.3.1, the phase diagram in 2.3.3, and the EoSs in Sec. 2.3.4.

2.3.1 Solver

Solving the ordinary differential equations (ODE), Eq. 2.1-2.4, is a two-point

boundary value problem (Press et al. 2007). We have a total of three differential equations for r , P , and T versus the independent variable m . P and T need to satisfy boundary condition at $m = M_p$, and the boundary condition for r is located at $m = 0$. The density may be discontinuous at a phase boundary whose location is unknown. Therefore, in our case, MAGRATHEA solves this problem with the method of shooting to a fitting point which is preferred to a relaxation method because it does not require

³*GNU Scientific Library* can be found at

<http://www.gnu.org/software/gsl/> 27

predefined grids.

MAGRATHEA integrates ODEs using GSL's *gsl odeiv2* (Galassi et al. 2009) with a Runge Kutta-Fehlberg method, which is a fourth order integrator with a fifth order error estimator and an automated adaptive step-size. To have a better estimation on the boundary conditions, $P(m = 0)$, $T(m = 0)$, and R_p , we conduct an extra round of iteration using a “pure” shooting method. In this first iteration, the ODEs are integrated from an estimated planet radius R_p at M_p outside-in toward the center until $m = 0$ or $P(m) > 10^5$ GPa. The R_p , which is the only unset boundary condition at M_p , is iterated using Brent-Dekker root bracketing method. The initial estimated radius is calculated based on a crude density assumption for each layer (15, 5, 2, and 10^{-3} for iron, mantle, ice, and atmosphere respectively in the unit of g cm^{-3}).

Predetermined by the user, the values of the enclosed mass at each layer interface are set as the bounds of the ODE integrator. In contrast, the enclosed mass where the phase changes within a layer is determined by the phase diagram in P - T space. Thus,

the step of the ODE integral typically does not land exactly on the location of the phase change. To avoid introducing extra inaccuracy, when the ODE integration reaches a different phase the integrator is restored to the previous step and the integration step is cut into half. The integrator can only move forward to the new phase when the step size that crosses the phase boundary is less than the ODE integrator accuracy tolerance multiplied by M_p .

Using the estimated boundary condition, we conduct the shooting to a fitting point method, which start ODE integration from both $m = 0$ and $m = M_p$ toward a fitting point with mass $m_{fit} = 0.2M_p$. The code will automatically adjusted m_{fit} if it occurs at a layer's boundary. The code uses GSL's *gsl multiroot fsolver hybrids* to adjust $P(0)$, $T(0)$, and R_p , until P , T , and r at m_{fit} obtained integrating from the inner branch and from the outer

branch agrees within a 28

Table 2.1: List of status information of the planet profile object

Value Meaning

0 Normal.

1 The result includes phase(s) that is(are) not formally implemented in MAGRATHEA.

2 The two shooting branches do not match within the required accuracy at the fitting point.

3 Under two-layer mode, the error of planet surface pressure is larger than the required accuracy.

relative error $<10^{-4}$. The ODE integrator tolerance will be reduced (made more strict) by a factor of three if the multidimensional root-finder can not find a solution within 15 tries. After the ODE integrator tolerance is reduced four times (three additional times, each by the stated factor of three), if the solver still cannot find a solution that satisfies the

required joint accuracy at the fitting point, the code will output an error message as well as the best result it can find.

The solver returns a planet interior profile object after completion, which includes the r , P , T , m , ρ , and the component phase at each grid step. A *print* function is available to save the profile into an ASCII table. The function *getRs* returns the list of radii of the outer boundary of each component. Users can use *getstatus* to access the status information of the returned object which indicates whether precautions should be taken regarding the iteration result. A list of potential problems and their assigned return value is summarized in Table 2.1.

2.3.2 Simplified Two Layer Mode

In addition to the regular solver, we include a mode for a simplified two layer solver. We use this for quick calculations of water/mantle and mantle/core planets in Huang et al. (2021). We recommend using our complete solver in most instances, but this method can be used for quicker

29

and cheaper calculations; one such use is demonstrated in Sec. 2.5.3.

Two-layer mode can only calculate the structure of 300 K isothermal planets and does not support an atmosphere. Without the temperature differential equation, the program only solves the radius and pressure differential equations, with the radius boundary condition at the center, and the pressure boundary condition at the surface. This simpler problem is solved using the "pure" shooting method inside-out, starting from the equations' singular point at the planet center. The solver iterates the center

pressure using the Brent-Dekker root bracket method until either the center pressure reaches the set accuracy target, or the surface pressure $P(M_p)$ is within 2% of the user specified value. If the iteration ends because the first criteria is satisfied first, an abnormal status value 3 will be returned by *getstatus*. To avoid this, users may adjust the ODE integration tolerance and center pressure accuracy target accordingly based on the specific problem.

With this solver, the two-layer input modes provide an interface to calculate mass-radius curves for hypothetical planets that are composed of only two components with fixed mass ratio (e.g. figure 3 in Huang et al. (2021)).

2.3.3 Phase Diagram Implementation

Phase diagrams are defined in *phase.cpp*. The file contains four functions corresponding to the four layers: *find Fe phase*, *find Si phase*, *find water phase*, and *find gas phase*. The *if* statement is used within each function to create the region of P-T space to which an EoS applies. The return value of each *if* statement should be the name of the pointer corresponding to the EoS for the given phase (further described in Appendix 2.6).

Transitions can be defined as pressure or temperature conditionals. Our default

phase diagrams 30

are shown in Fig. 2.2. We use phase transitions which are linear with pressure/temperature within the conditionals for the transfer between solid and liquid

iron (Dorogokupets et al. 2017) and between bridgmanite and post-perovskite (Ono & Oganov 2005). Parameterized phase transition curves can also be defined as separate functions in *phase.cpp* and called within the “find phase”

functions. We define the function *dunaeva phase curve* to implement the fitting curve with five coefficients, $T(P) = a + bP + c \ln P + d/P + e \sqrt{P}$, from Dunaeva et al. (2010) for the transitions

between phases of water.

2.3.4 Built-In Equations of State

We have over 30 EoSs available in MAGRATHEA which can be called within the phase diagrams. These include EoS functions for various planet building materials, and different parameter estimates for the same material from various works. We discuss the equations currently available for each layer in the following four subsections. New EoSs can be added to *EOSlist.cpp* by following the storage structure described in Appendix 2.6. In Fig. 2.3 we show mass-radius relationships up to ten Earth-masses for planets of one layer with a large selection of our implemented equations. The index of equations in Fig. 2.3 is also noted in the text in brackets.

In addition to the equations listed below, the program includes tabulated EoS of iron, silicate, and water from Seager et al. (2007) [CS, MS, WS], who combined empirical fits to experimental data at low pressure and Thomas-Fermi-Dirac theory at high pressure.

31

WD		MD	100% water	0
WS	2.50	MD-2000	CD	
W1		MS	CD-2000 CS	-5
W2	2.25	MP	C1	C2
	W3	M1	5	CW1 CW2
	W4	M2		
			5	
			2 4 6 8 10	
			1.75	
2.00			0	
	100%	mantle		
1.50			-5	
				2 4 6 8 10
1.25	100% core			
1.00			5	
0.75			0	
	2 4 6 8 10 M		-5	2 4 6 8 10 M

Index Description Source

*D Default EoSs Multiple

*S Tabulated Seager et al. (2007)

*-2000 2000 K surface Multiple

WD Ice VI & VII Bezacier et al. (2014)

Ice X Grande et al. (2022)

W1 Ice VII Frank et al. (2004)

Ice X French et al. (2009)

W2 Ice VII Frank et al. (2004)

W3 Ice VII, VII', X Grande et al. (2022)

W4 Ice VI & VII Bezacier et al. (2014)

Ice X Hermann & Schwerdtfeger (2011)

MD Brg Oganov & Ono (2004)

PPv Sakai et al. (2016)

MP PREM Zeng et al. (2016)

M1 Brg/PPv Oganov & Ono (2004)

M2 Brg Shim & Duffy (2000)

CD Fe HCP Smith et al. (2018)

C1 Fe HCP Bouchet et al. (2013)

C2 Fe HCP Dorogokupets et al. (2017)

CW1 Fe-7wt%Si Wicks et al. (2018)

Figure 2.3: *Top*, mass-radius relationship for planets with 100 per cent of mass in either the core, mantle, or hydrosphere demonstrating many of the EoSs implemented in MAGRATHEA. *Bottom*, percent difference in final planet radii compared to our selected “default” EoSs for water (*top*), mantle (*middle*), and core (*bottom*). Table lists the major components of each model with 300 K surface temperature unless designated with a “-2000”. Near the surface, water planets have water and Ice VI, and hot mantle planets have silicate melt.

2.3.5 Core/Iron

At the extreme pressures of a planetary core, iron is stable in a hexagonal close-packed (HCP) phase. The program includes HCP iron EoSs from Bouchet et al. (2013) [C1], Dorogokupets et al. (2017) [C2], and Smith et al. (2018) [CD] (see Fig. 2.3). We choose as our default equation the Vinet fit (Eq. 2.9) from Smith et al. (2018) measured by ram compressing iron to 1.4 TPa. We determine the fitting parameters of the Gruneisen by fitting Eq. 2.13 to Fig. 3b in Smith et al. (2018) through maximum likelihood estimation. The default core layer includes a liquid iron EoS and melting curve from Dorogokupets et al. (2017) who compressed iron to 250 GPa and 6000 K.

Iron-silicate alloy EoSs are implemented as well. Wicks et al. (2018) experimentally determined the EoS for Fe-Si alloys with 7 wt per cent Si [CW1] and 15 wt per cent Si [CW2]. These alloy equations are useful in reproducing the density of the Earth’s core which contains an unknown mixture of light elements (Hirose et al. 2013). An additional liquid iron equation is included from Anderson & Ahrens (1994).

At lower temperatures and pressures, fcc (face-centered cubic) iron is not currently implemented. The EoS of fcc iron has similar parameters to that of hcp iron ($K_{0,fcc} = 146.2$, $K_{0,hcp} = 148.0$). The fcc-hcp-liquid triple point is at 106.5 GPa and 3787 K

(Dorogokupets et al. 2017).

2.3.6 Mantle/Silicate

The main mineral constituent of the Earth's mantle is bridgmanite (Brg), referred to in the literature cited here as silicate perovskite, which at high pressure transitions to a post-perovskite (PPv) phase (Tschauner et al. 2014). MAGRATHEA includes third-order BME (Eq. 2.8) Brg from Shim & Duffy (2000) [M2] and Vinet EoSs (Eq. 2.9) for Brg and PPv measured with *ab initio*

33

simulations and confirmed with high pressure experiments from Oganov & Ono (2004) and Ono & Oganov (2005) [M1].

Our default mantle [MD] includes Brg from Oganov & Ono (2004) and an updated PPv thermal EoS from Sakai et al. (2016). Sakai et al. (2016) compressed PPv to 265 GPa with a laser-heated diamond anvil cell and extended the EoS using a Keane fit (Eq. 2.11) to 1200 GPa and 5000 K with *ab initio* calculations. At high temperatures (>1950 K at 1.0 GPa), we use a liquid MgSiO_3 with RTPress EoS from Wolf & Bower (2018) with melting curve from Belonoshko et al. (2005b). The silicate melt transfers directly to PPv when $P > 154$ GPa and $T > 5880$ K since the behavior in this regime is unknown. An alternate silicate melt is implemented from Mosenfelder et al. (2009).

Our default mantle is thus pure MgSiO_3 in high-pressure phases which is more SiO_2 rich than the Earth. At low pressure (≤ 25 GPa), materials such as olivine, wadsleyite, and ringwoodite are the main constituents (Sotin et al. 2007). Although we don't include

these minerals and more complex mantle chemistry at this time, we include a tabulated EoS for the mantle using the mantle properties in the Preliminary Reference Earth Model (PREM) (Stacey & Davis 2008; Appendix F) [MP]. We also have not explored additional measurements of transition curves between compositions/phases.

2.3.7 Hydrosphere/Water

Similar to the icy moons in the Solar System; exoplanets with low density are theorized to have a large fraction of mass in a hydrosphere composed of primarily high-pressure water-ice. Laboratory measurements of the thermal properties of ice at high pressures are difficult to obtain and sometimes inconsistent (Thomas & Madhusudhan 2016; Myint et al. 2017). Due to the complex

34

ity of the phase diagram of water and large uncertainties in current measurements, in the current version of MAGRATHEA, we use a simplified hydrosphere phase diagram. At pressures below 2.216 GPa, we applied liquid water (Valencia et al. 2007b) if the temperature is above the melting curve (Dunaeva et al. 2010). Below the melting curve, we have Ice Ih (Feistel & Wagner 2006; Acuna et al. 2021) at pressures below 0.208 GPa and Ice VI (Bezacier ~ et al. 2014) (described below) at pressures above 0.632 GPa. Ice II, III, and V, which exist at pressures in between, are currently not built-in since this layer is thin and has negligible impact on the planet. If a planet passes through these phases, the Ice VI EoS is used and the user is notified that they passed through this region. For water and Ice Ih the isothermal temperature is applied regardless the value

of the *isothermal* flag.

At high pressure, our default hydrosphere layer uses Ice VII with thermal expansion (Bezacier et al. 2014). Instead of using the MGD representation, most high pressure ice studies express their result with thermal expansivity, with the exception of Fei et al. (1993) which present their result with both methods. Although the isobaric specific heat capacity c_p is necessary to determine the temperature gradient using the thermal expansivity representation (see Eq. 2.5), it is not reported in most studies. Similar to Zeng et al. (2021), we include a formulation using the thermal expansion representation for Ice VI and VII from Bezacier et al. (2014) with estimated c_p of 2.6 and 2.3 J g⁻¹ K⁻¹ based on Tchijov (2004).

At this time, we do not include a phase boundary or EoS for supercritical water. To avoid extrapolating the Ice VII EoS to high temperature that may lead to non-physical density, an artificial melting curve at constant temperature 1200 K is drawn in between 2.216 GPa and 30.9 GPa. The water EoS (Valencia et al. 2007b) is used as an approximation in supercritical regions and the user is notified. Lastly, the default hydrosphere transitions at 30.9 GPa to a Vinet EoS for Ice X from 35 Grande et al. (2022) which is calculated at 300 K and returns a constant temperature throughout regardless the value of the *isothermal* flag.

The following high-pressure water-ice EoSs are also available as alternative. Third-order BME Ice VII EoS with thermal expansion and heat capacity from Frank et al. (2004) and 3rd order BME Ice VII EoS using MGD expression from Sotin et al. (2007). Other ice EoSs that implemented do not support the isentropic temperature gradient. They include Ice VII EoS along the melting curve (Frank et al. 2004) and tabulated Ice X

(French et al. 2009) which combined were used in the planetary models of Zeng et al. (2016) [W1]. Our library has three fits to the 300 K Ice VII measurements from Frank et al. (2004) – their original 3rd order BME, their BME parameters in a Vinet equation [W2], and a Vinet fit to their results. We have the three phases of ice including the transitional Ice VII' from Grande et al. (2022) which was used in Huang et al. (2021) [W3]. Lastly, we have a 3rd order BME Ice X from Hermann & Schwerdtfeger (2011) [W4]. A future version of MAGRATHEA will expand upon these options with results from French & Redmer (2015), Journaux et al. (2020), and other water phases from the AQUA collection (Haldemann et al. 2020).

2.3.8 Atmosphere/Gas

The ideal gas equation of state:

$$P = \rho RT \quad m_{mol} \quad (2.31)$$

and temperature relation:

$$T \propto P^{(\gamma_{gas}-1)/\gamma_{gas}} \quad (2.32)$$

36

is applied to the gas layer at all pressures and temperatures, where γ_{gas} is the adiabatic index of the gas. Combining Eq. 2.1, 2.2, 2.31, and 2.32, we have the ideal gas temperature gradient

$$dT(m)$$

$$dm = -(Y_{\text{gas}} - 1)m_{\text{mol}}Gm$$

$$4\pi r^4 Y_{\text{gas}} R \rho. \quad (2.33)$$

The temperature profile can be chosen between isothermal and isentropic by setting the number of atoms per molecule n (see Table 2.5), which further determines Y_{gas} . The adiabatic index γ_{gas} can be chosen from $\gamma_{\text{gas}} = \frac{5}{3}$ for monatomic gas, $\gamma_{\text{gas}} = \frac{7}{5}$ for diatomic gas, and $\gamma_{\text{gas}} = \frac{4}{3}$ for polyatomic gas. An isothermal gas EoS can be achieved by setting its $n = 0$. The temperature profile of the gas layer is determined by the properties of the gas EoS and will not be overwritten by the *isothermal* flag.

Nixon & Madhusudhan (2021) shows that self-consistently modelled atmosphere temperature profiles can be closely matched by a radiative profile above a radiative-convective boundary, and an adiabatic profile below the boundary. The pressure of the radiative-convective boundary can span from 1 bar to over 1 kbar, mainly depending on the intrinsic effective temperature and equilibrium temperature of the planet (Fortney et al. 2007). To simulate this temperature structure, the default settings for the atmosphere in MAGRATHEA include an isothermal atmosphere at $P < 100$ bar to approximate the radiative temperature gradient, and an adiabatic temperature gradient at $P \geq 100$ bar. The mean molecular weight of each gas EoS is fixed. The dependence of planetary radius on atmosphere mean molecular weight is explored in Fig. 2.7.

Radiative temperature profile and coupled atmosphere-interior models such as Mousis et al. (2020) are potential future avenues of work. Additionally, we anticipate that future versions of MAGRATHEA will include non-ideal atmospheres from Saumon et al.

(1995) and Chabrier et al.

(2019).

2.4 Known Limitations

We design MAGRATHEA with a focus on extensibility. MAGRATHEA permits users to extrapolate EoS functions beyond the temperature and pressure bounds from experimental and theoretical works. The phase diagram can be set up to allow a material where it would not be physical (e.g. use water in place of supercritical water). If the integrator passes through these extrapolated regions, it may find an incorrect solution or may fail to continue to integrate. Here we detail some limitations one should be aware of for each layer with our current defaults.

For the core, the liquid iron EoS from Dorogokupets et al. (2017) has no solution when the temperature of a given step gives a thermal pressure much larger than the total pressure at that step. This occurs most often when the iron core outer boundary is near the surface of the planet and at unusually high temperatures. In this case, a *no solution found* tag will be returned.

Extrapolated EoS functions may have two density solutions that satisfy the equation set at given P and T . The nonphysical solution typically has a lower density and the $\frac{\partial \rho}{\partial P} < 0$.

The Newton's method density solver may converge to the incorrect branch at a transition from a low density phase to a higher density phase because the initial density guess of the high density phase is too small. We experienced this problem in the mantle when

transitioning from Si melt to Brg from Oganov & Ono (2004) at low pressures. To avoid this, if the initial density guess gives $\frac{\partial \rho}{\partial P} < 0$, a density

larger than $\rho(P = 0, T = T_0)$ will be applied as the initial density guess of the Newton's solver, instead of the density solution of the previous step.

For the hydrosphere, users should be aware that MAGRATHEA will use the water EoS

and return 38

a constant temperature even if the water would be in the vapor or supercritical phase. Because water EoS is softer and the thermal expansion is not included, the density is overestimated in supercritical regions. This may lead to a density drop at the phase transition from supercritical fluid to Ice X. Other phases without thermal parameters, such as Ice X, will return a constant temperature. Lastly, the adiabatic portion of the default atmosphere quickly rises in temperature and pressure and could force internal layers into extreme regions of the phase diagram. Ideal gas atmospheres with constant mean molecular weight are less realistic for large gas envelopes with pressures over 0.1 GPa (Zeng et al. 2021; Nixon & Madhusudhan 2021).

2.5 Test Problems and Utility

2.5.1 One-Earth Mass and Comparison with ExoPlex

We turn our attention to showing the outputs and utility of MAGRATHEA. We first simulate a one-Earth mass, two-layer planet with our full solver. The planet has a

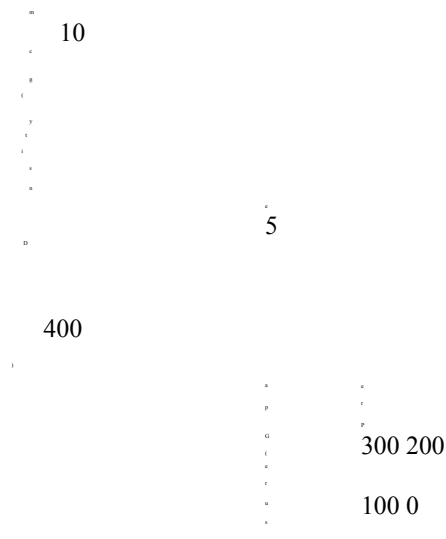
structure similar to Earth with 33 per cent of its mass in the core (Stacey & Davis 2008). With the default EoSs described in Sec. 2.3.4 and a surface temperature of 300 K, MAGRATHEA produces a planet with radius of 6166 km or 0.967 R_{\oplus} . Fig. 2.4 shows the pressure, density, and temperature found throughout the planet.

Our default model differs from a detailed model of Earth in that our mantle is only Brg/PPv, the core has no lighter elements, and there is thermal equilibrium between the layers. Rather than choosing our default settings, users can choose to use an iron-silicate alloy EoS (Wicks et al. 2018) in the core and PREM in the mantle. The user can also start the mantle hot at 1600 K and implement a 2900 K jump across the core-mantle boundary which creates a layer of liquid iron.

Magrathea Default
0.9668 R 0.692 s
Magrathea Adjusted
0.9884 R 0.259 s
15

39

ExoPlex
0.9978 R 1.46 s



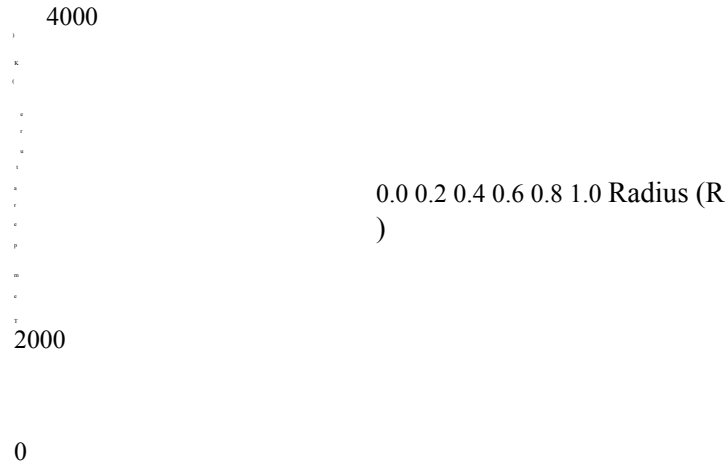


Figure 2.4: Density, pressure, and temperature verses radius solution for a two-layer, one Earth mass planet with 33 per cent by mass core. The three models shown are *Magrathea Default* with hcp-Fe core (Smith et al. 2018) and Brg/PPv mantle (Oganov & Ono 2004; Sakai et al. 2016), *Magrathea Adjusted* with Fe-Si alloy core (Wicks et al. 2018) and PREM mantle (Zeng et al. 2016) and a temperature discontinuity, and the default settings in *ExoPlex*. *Magrathea Default* is set to 300 K at the surface while *ExoPlex* suggests a 1600 K mantle. Temperature is solved throughout *Magrathea Default* and in *ExoPlex*'s mantle. *Magrathea* returns no change in temperature when a phase does not have temperature parameters available while *ExoPlex* returns zero Kelvin. The planet's radius and the average run time over 100 integrations is listed in the legend.

40

This “adjusted” model, shown in Fig. 2.4, has a radius within 1.16 per cent of the radius of Earth ($0.9884 R_{\oplus}$).

We compare our Earth-like planets to one created with a version of *ExoPlex*⁴, an open-source interior structure solver written in Python. *ExoPlex* is used in Unterborn et al. (2018); Unterborn & Panero (2019); Schulze et al. (2021b). The code uses a liquid iron core (Anderson & Ahrens 1994) and self-consistently calculates mantle phases with *Perple X* (Connolly 2009) using EoS for mantle materials from Stixrude & Lithgow-Bertelloni (2005). *ExoPlex* comes with predetermined grids of mineralogy to

capture the mantle chemistry of planets between 0.1 and $\sim 2 M_{\oplus}$.

As seen in the top panel of Fig. 2.4, *ExoPlex* captures changes in density in the upper mantle that our Brg/PPv model does not. *ExoPlex* creates an Earth-like planet with a radius of $0.9978 R_{\oplus}$ which is 3.2 per cent larger than our default planet and 1.0 per cent larger than our adjusted model. At least half of this difference is from a different choice in core EoS; *ExoPlex*'s innermost density is 14.0 while our default is 14.8 g cm^{-3} . The rest of the difference is *ExoPlex*'s ability to capture upper-mantle chemistry which decreases the density from our default for approximately 15% of the planet's mass.

2.5.2 Run Time

We perform timing tests for both MAGRATHEA and *ExoPlex* for 100 repeat simulations of the Earth-like planet from the above section. MAGRATHEA takes on average 0.69 s to converge. This is 2.1 times faster than *ExoPlex* (1.46 s). The “adjusted” model uses a tabulated EoS for the mantle and a core EoS with no thermal information, thus most of the planet is isothermal with temperature only solved in the small region of liquid iron. This model runs 5.6 times faster than

⁴<https://github.com/CaymanUnterborn/ExoPlex>

2.00	1.00
1.75	0.75
1.50	0.158 0.5 1.58 5.0 15.8
1.25	50.0
	C:M:W:A Mass % 0:
	100: 0: 0

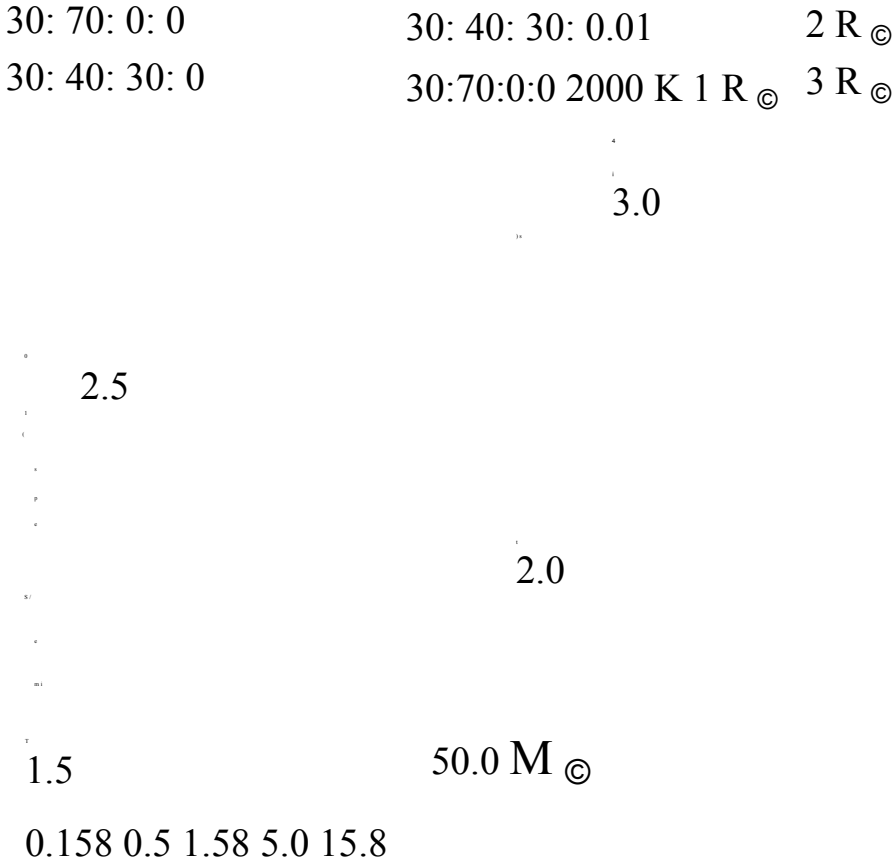


Figure 2.5: Plot of run time, *top*, and of run time divided total number of steps, *bottom*, for our default model across six planet masses and four compositions: 100% core, 30% core 70% mantle, 30% core 40% mantle 30% water, and 30% core 40% mantle 29.99% water 0.01% H/He atmo sphere with 300 K surface temperature. The last set of planets, *orange*, have 30% core, 70% mantle, and surface temperature of 2000 K. The run time is the average time measured across 100 runs. Sizes of the markers are proportional to the planet radius.

The run time of MAGRATHEA is dependent on the mass of the planet, the user's choice of planet model, and the error tolerances. In Fig. 2.5, we show run times of some typical planet masses and compositions with our default settings. Four compositions are run with a surface temperature of 300 K. A final set has a surface temperature of 2000 K

which has a region of silicate melt at the surface. The figure shows that time remains near one second, but is not easily determined by input mass and composition. Here the average run time is 1.2 seconds. The longest and shortest run times are a factor of 2.5 times slower/faster. These solutions take between 15 and 30 iterations, and the final solutions have between 520 and 840 steps in mass.

In general the run time increases with mass, though not strictly since the step size is adaptable. Crossing phase or compositional boundaries costs an insignificant amount of run time. However, certain phases may take shorter or longer to solve. The planets with atmospheres have the most compositional layers, but the ideal gas solves quickly resulting in the shortest time per step. The runs which take the longest to converge are large, hot planets with a surface of silicate melt and large mantles.

2.5.3 Uncertainty from Equation of State

MAGRATHEA's structure allows the user to change the EoS and test their effects on planet structure. In Fig. 2.3, we show how choice of EoS can change the radius of single layer planets of masses from one to ten Earth-masses. For the hydrosphere, further discussed in Huang et al. (2021), new measurements of Ice VII, Ice VIIt, and Ice X change the resulting planet radius from those in Zeng et al. (2016) by 1-5 per cent across this range of masses.

	Phase	TP	V_0	K_0	K'_0	σ_R/μ_R	for 10 M_\oplus	GPa	$\text{cm}^3 \text{mol}^{-1}$	GPa	GPa	%
Fe HCP	-	6.625	177.7(6)	5.64(1)	0.089	PPv	112.5(8.1)	24.73	203(2)			
		5.35(9)	0.19	ice-VII	-	12.80(26)	18.47(4.00)	2.51(1.51)				
ice-VII _t		5.10(50)	12.38(16)	20.76(2.46)	4.49(35)	0.24	ice-X	30.9(2.9)				
		10.18(13)	50.52(16)	4.5(2)								

The mantle's EoS has the smallest effect on radius in agreement with Unterborn & Panero (2019). Comparing the tabulated EoS from PREM to our default mantle, we find that the radii of pure mantle planets differ by less than one percent for 2-5 M_\oplus . Planets <2 M_\oplus have a larger difference in simulated radii. Capturing the density of the upper mantle is more important for these smaller planets.

HCP iron measurements generally agree when looking at bulk planet properties. However, it is uncertain how much lighter elements can be incorporated into a planet's core. Included in MAGRATHEA are two silicate alloy EoSs from Wicks et al. (2018). Using a 15 per cent by weight silicate alloy EoS results in a 1 M_\oplus , core-only planet that differs by five per cent in radius to our default. For comparison to the above radius changes, the 1-sigma uncertainties in radii of the seven Trappist-1 planets are 1-2 per cent (Agol et al. 2021).

A single measured EoS also has uncertainties in its own parameters. MAGRATHEA includes the ability to modify an EoS at run-time to determine the effects that measurement uncertainty has on a planet radius estimates. This feature is available in *input mode* 3, 4, and 5. It's implementation is further detailed in Appendix 2.7. The first two modes are limited to using the isothermal *twolayer*

solver explained in Sect. 2.3.2. The *input mode=5* runs the full model with user specified planet composition and mass. MAGRATHEA iterates over EoS parameters from an input file and outputs the planet radius for each EoS modification.

In Table 2.2, we show the reported uncertainties in three experimental EoS from Sakai et al. (2016); Smith et al. (2018); Grande et al. (2022). We model 10 M_{\oplus} planets each with a single layer. We then modify the EoS of that layer from 1000 values of the reference volume, bulk modulus, and the derivative of the bulk modulus drawn from Gaussians centered at the reported mean and using the given uncertainties. For the 100 per cent mantle and 100 per cent hydrosphere models we also draw 1000 values of the transition pressure (TP) between phases. The mantle planets have a Brg phase, but it's parameters are held constant as they are derived from *ab initio* simulations. The resulting uncertainty in planet radius for each single-layer model is < 1 per cent for 10 M_{\oplus} planets. Although the choice of EoS is of more consequence to a single measurement's uncertainty, this module allows users to investigate new measurements and their associated uncertainties.

2.5.4 Ternary Diagram

In Section 2.3.4, we show mass-radius relationships for single-layer planets. However, these relationships are not unique when considering a planet with three or more layers.

For a three layer planet, ternary diagrams provide a way to visualize the radius parameter space for a planet with a certain mass (conversely we could show the various masses for a certain radius). Ternary diagrams have been used for exoplanet interiors in Valencia et al. (2007a), Rogers & Seager (2010), Madhusudhan et al. (2012), Brugger et

al. (2016), Neil & Rogers (2020), and Acuna et al. (2021). ~ The location of a point on the equilateral triangle is given by the percentages of mass in the

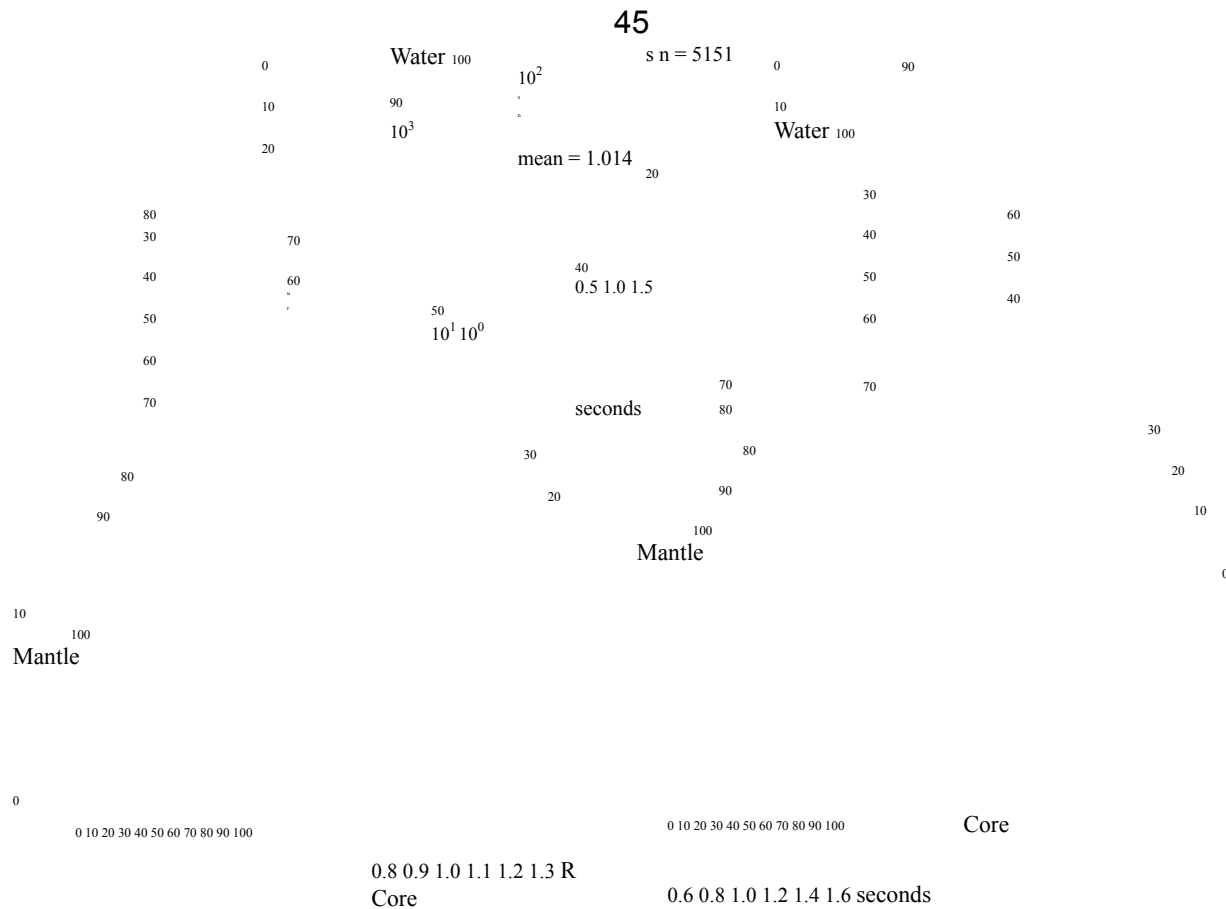


Figure 2.6: *Left*, ternary diagram where the axes are the percentage of mass in a core, mantle, and water/ice layer. The radius in Earth radii is shown by the color scale for 5151, one Earth mass planets at integer percentages with our default model. Color map is interpolated between the simulations. *Right*, plot of MAGRATHEA's run time for each planet. *Middle*, histogram of run time on a log-log scale showing mean time of 1.014 seconds. Ternary plots are generated with the python-ternary package by Harper et al. (2015) with colormaps from Van der Velden (2020).

three layers—core, mantle, and water. The three coordinates add to a constant 100%. Since axes are interchangeable, we decide to use the same representation as Zeng & Seager (2008). With this orientation the core to mantle ratio increases along the bottom axes and the water percentage increases perpendicular to the bottom axis.

We include with MAGRATHEA, a ternary plotting python script that uses python-ternary by Harper et al. (2015). To run 5151 planets with integer percentages of mass in each layer we use MAGRATHEA's bulk input mode (*input mode=6*). This function requires an input file that contains each planet's total mass and the mass fraction of core, mantle, and hydrosphere. Any mass not allocated to a layer is put into an atmosphere layer.

In Fig. 2.6 *left* each position on the triangle gives the radius of a unique one Earth-mass planet. We use planets in thermal equilibrium, a 300 K surface temperature, and with our default EoSs. This model underestimates the Earth's radius as discussed in Sec. 2.5.1. A dry, one Earth-mass, and one Earth-radius planet in these simulations has approximately a 19 per cent core mass fraction (cmf). Because of the difference between water's and iron's density, we can see that the radius varies most dramatically along the water-core axis. A one Earth-mass and Earth-radius planet is also consistent

with having 75 per cent cmf and 25 per cent of mass in a hydrosphere.

The entire suite of simulations needed for the one Earth-mass ternary takes approximately 87 minutes to complete. The time for each run is shown in Fig. 2.6, *right*. The average run time is 1.014 seconds. In agreement with Fig. 2.5, time has a weak correlation with mantle percentage.

47

no atm	0		
CO2	10		
H2O	20		
H/He	30		
	40		
	Water		
50	100		20
60	90	40	10
70	80	30	
80	70	6000 km	7000
90	60	8000	
100	50	9000	

Mantle
Core

Figure 2.7: Core-Mantle-Water mass percentage ternary plot with colored contours of constant radius for one Earth-mass planets. Four types of planets, represented by the line-style, are calculated: one with no atmosphere and three with 0.01 per cent of their mass in an atmosphere layer. The atmosphere mass was subtracted equally from both the mantle and core to keep total mass equal to one Earth-mass. The three atmospheres have varying mean molecular weight: CO_2 with 44 g mol^{-1} , H_2O with 18 g mol^{-1} , and H/He mixture with 3 g mol^{-1} .

2.5.5 Ternary with Atmosphere

As a final example, we add an atmosphere to our ternary planets using our default two “phase” ideal gas atmosphere. In Fig. 2.7, we show contour lines of constant radius. The solid lines come from Fig. 2.6. The 5151, one Earth-mass planets are simulated again with 0.01 per cent of their mass taken equally from the core and mantle and put it into an atmosphere layer. This is comparable to the atmospheric mass fraction of Venus. Three types of ideal gas are used with varying molecular weight.

A small atmosphere of a hydrogen/helium mixture inflates the planets by almost 1000 km for all interior structures. A 6000 km, one-earth mass planet with a small H/He atmosphere is consistent with a 2-layer planet of 20:80 mantle:core (intersection of mantle-core axis, bottom) or 5:95 water:core (intersection of core-water axis). Together, the one Earth-mass ternaries explore the radii of a large range of possible interior (plus atmosphere) structures.

2.6 EoS Storage Structure

Calculating the density for a variety EoS formulae or tabulated EoS is packaged in the structure *EOS* declared in *EOS.h* and accomplished in *EOS.cpp*. The EoS of each phases needed for the calculation is an object of the *EOS* structure.

The name of pointers to *EOS* objects should be declared as an external variable in the header file *EOSlist.h* and then accomplished in *EOSlist.cpp*. To use the formula method, user should create a dictionary style two-dimensional double array with a shape of $(length, 2)$, where *length* is the number of provided EoS parameters. Table 2.3 - 2.5 explains all acceptable parameters. In the array, the first number of each row is the index key of the parameter according to Table 2.5. The

49

Table 2.3: Index for types of isothermal EoS formulae

Index	Function Name	Comment
0	BM3	3rd order Birch-Murnaghan ^a
1	BM4	4th order Birch-Murnaghan
2	Vinet	
3	Holzappel	
4	Keane	
5	Empty	
6	Ideal gas law	
7	Interpolation	
8-12	Same as 0-4	In combination with RTPress

^a Default

second number is the value in the required unit. Not all spaces in the table need to be filled up. Not available values can be skipped. V_0 and m_{mol} are required for all types of

EoSs. K_0 is required for condensed phase material. γ_0 and β are required for isentropic temperature profile and thermal expansion. The minimum required parameters can be determined by the corresponding formulae listed in Section 2.2.2 and default values in Table 2.5.

Then the EoS object pointer can be constructed using the EoS constructor that have three arguments. The first one is a string of the phase description, then is the name of dictionary style double array, and the third argument is *length*, the number of parameters provided. The name of the EoS object pointer should be the same as the one declared in *EOSlist.h*.

The following shows the EoS of post-perovskite phase of MgSiO_3 in the code as an example. Code in *EOSlist.h*

```
// Declare pointers to EoS objects
extern EOS * SiPPvSakai;
```

Code in *EOSlist.cpp*

50

Table 2.4: Temperature profile option ^a

Index Temperature profile calculation method

0 No temperature profile, must be
isothermal 1 External entropy function
2 External temperature gradient function

^b 3 Ideal gas

4 EoS is fitted along isentrope ^c

5-7 Isentropic curve ^d

8 RTPress

9 Thermal expansion ^e

^a Only need to specify this option in the input list if using external entropy function or external temperature gradient function

(index 1 or 2), or the EoS is fitted along isentrope (index 4). Otherwise, the code will determine the option based on the parameters provided.

- ^b The only method to set the gradient is using the modify `extern dTdP` function.
- ^c Selecting this option requires parameters to calculate Debye thermal pressure in Eq. 2.15. The isentrope temperature profile is enforced to the phase with this option even the isothermal option is chosen for the planet solver.
- ^d Selecting this option requires parameters to calculate Debye thermal pressure in Eq. 2.15.
- ^e Selecting this option requires α and c_p .

Table 2.5: List of EoS parameters

Index	Variable	Unit	Comment
0	EoS formula type		
1	V_0	$\text{cm}^3 \text{mol}^{-1}$	
2	K_0	GPa	
3	K'_0		
	Default	4	
4	K''_0	GPa^{-1}	
5	m_{mol}	g mol^{-1}	
6	P_0	GPa	
7	Θ_0	K	
	Default	1	
8	γ_0		
9	β		
	Fitting parameter of Gruneisen (see Eq. 2.13 and 2.24)		
10	γ_∞		
	Fitting parameter of Gruneisen (see Eq. 2.14).		
	Default	2/3	
11	γ'_0		
12	e_0	10^{-6}K^{-1}	

Helmholtz Electronic contribution (see Eq. 2.12).

Default 0 13 g

Electronic analogue of the Gruneisen (see Eq. 2.12) "

14 n

Number of atoms in the chemical formula ^a. Default 1

15 Z

16 T_0 K

Reference temperature (see Eq. 2.7). Default 300

17 $\alpha_0 10^{-6} \text{K}^{-1}$

The zeroth order coefficient of thermal expansion

at a P_0 18 $\alpha_1 10^{-6} \text{K}^{-2}$

The first order coefficient of thermal expansion at P_0

19 ξ

Power law index for thermal expansion (Eq. 2.28). Default 0

20-22 $c_{p0} 10^7 \text{erg g}^{-1} \text{K}^{-1}$ Coefficients for specific heat capacity at
constant pressure (see Eq. 2.30) 23 Debye approx

Positive number for Debye, otherwise Einstein

24 thermal type

See table 2.4

^a Number of atoms in the volume of V/N_A , where N_A is the
Avogadro constant. The n of ideal gas is the number of atoms
per molecule for the purpose of adiabatic index.

52

```
\\ Dictionary style double array
```

```
double SiPPvSakaiarray[][2]
```

```
= { {0,4}, {1,24.73}, {2,203}, {3,5.35},
```

```
{5,mMg+mSi+3  
*mO}, {8,848}, {9,1.47},
```

```
{10,2.7}, {11,0.93}, {15,5}};
```

```
\\ Create a EOS object pointer
```

```
EOS  
*SiPPvSakai
```

```
= new EOS( " Si PPv ( S a k a i ) ",
```

```
SiPPvSakaiarray,
```

```
sizeof(SiPPvSakaiarray)/2
/sizeof(SiPPvSakaiarray[0][0]));
```

For RTpress EoS framework, a list of additional polynomial fitting terms b_n , in the unit of erg mol^{-1} , are required (see Eq. 2.21). A separate array and its size *blength* are used to construct a RTpress EoS object. The following shows the EoS of liquid MgSiO_3 as an example. Code in *EOSlist.h*

```
extern EOS
* SiLiquidWolf;
```

Code in *EOSlist.cpp*

```
double SiLiquidWolfarray[][2]
= { {0,10}, {1,38.99}, {2,13.2}, {3,8.238},
{5,mMg+mSi+3
*mO}, {9,0.1899}, {10,0.6},
{12,-1.94}, {15,5}, {17,3000} };
```

53

```
double SiLiquidWolfb[]
= {4.738 E12, 2.97 E12, 6.32 E12,
-1.4 E13, -2.0 E13 };
```

```
EOS
* SiLiquidWolf
= new EOS(" SiLiquid ( Wolf )",
SiLiquidWolfarray, SiLiquidWolfb,
sizeof(SiLiquidWolfarray)/2
/sizeof(SiLiquidWolfarray[0][0]),
```

```
sizeof(SiLiquidWolfb)
/sizeof(SiLiquidWolfb[0]));
```

2.7 Modify a Built-In EoS in Runtime

Once an EoS is built-into the code, it is possible to modify its parameter in the run-time without the request of recompile the full code. This feature is useful to rapidly repeat runs with similar EoS parameters, for example when study the impact of the uncertainty of EoS parameters on planet size. One can modify one parameter of a EoS using

```
void EOS::modifyEOS
(int index, double value),
```

where index is listed in Table 2.5. Or using

```
void EOS::modifyEOS
(double params[][2], int length)
```

54

to modify multiple parameters at once, where length is the number of parameters that need to be modified and params is the dictionary style 2D double array (see Appendix 2.6). If the phase boundary between phases are independent of temperature and purely determined by the pressure, e.g. the phase boundary commonly assumed between ice VII and ice X, the phase transition pressure within a layer can also be modified using

```
void setphasehighP
(int k, double *startpressure,
```

EOS
** phase name) ,

where k is the number of phases involved in this modification, *phase name* is an array of EoS pointers of these k phases, and *start pressure* is the array of phase transition pressures between these k phases in the unit of GPa with a length of $k-1$. If the name of the first EoS in the *phase name* EoS list matches the name of one of the original EoS of this layer, the first input EoS will replace the original one. Otherwise, the first EoS in the list will be ignored in the calculation.

External EoS function, entropy function, or temperature gradient function can be modified using

```
void modifyexterndensity
```

```
( double ( * f ) ( double P , double T ) ) ,
```

```
void modifyexternentropy
```

```
( double ( * g ) ( double rho , double T ) ) ,
```

or

```
void modifydTdP
```

```
( double ( * h ) ( double P , double T ) )
```

55

respectively.

2.8 Summary

In this chapter, I presented MAGRATHEA, an open-source planet interior solver, as

collaborators and I published in Huang et al. (2022). MAGRATHEA is available at <https://github.com/Huang-CL/Magrathea>. Given the mass in the core, mantle, hydrosphere, and atmosphere, the code uses a shooting method to find the planet's radius and internal conditions.

The code allows users to easily modify their planet models. Each layer is given a phase diagram where the EoS may change based on P-T conditions. Multiple formulations, both thermal and non thermal, for the EoS are implemented. We document in this work our built-in library of EoSs and how to add new equations. Our default EoSs feature up-to-date experimental results from high pressure physics. We show that the choice of planet model has an effect on inferences of planet composition.

The timings and results presented here show that MAGRATHEA is an efficient and useful tool for characterizing the possible interiors of planets. MAGRATHEA is currently under active development and we plan future expansions to the package. In this version, the isentropic temperature gradient is only available for the Ice VI and Ice VII in the hydrosphere. Further development of the code is detailed in Ch. 3 while expansions of the EoS library is described in Ch. 4. We describe future developments in the summary sections of each chapter. We encourage the community to contribute and use MAGRATHEA for their interior modeling needs.

Further MAGRATHEA Developments

3.1 Background

Open-source software is freely available for anyone to use, modify, and distribute. Anyone can easily access and use the software for their research. Although there are concerns about appropriate attributions, open-source resources remove the need for expensive licenses and proprietary restrictions. This accessibility can accelerate scientific progress.

In addition, open-source software is often more transparent and auditable than proprietary software. Because the source code is available, researchers can examine and modify the software to ensure it is working as intended and to adapt it to their specific needs. This transparency and accountability can increase the reliability and reproducibility of research.

Open-source software plays a critical role in astronomy. The open-source programming language, Python, is foundational to modern astronomy for data analysis. I use a number of open source Python packages in this work including PYTHON-TERNARY (Harper et al. 2015), NUMPY (Harris et al. 2020), MATPLOTLIB (Hunter 2007), and CMASHER (Van der Velden 2020). Other open-source tools commonly used in astronomy include the Image Reduction and Analysis Facility (IRAF, Tody 1986) and ALADIN (Bonnarel et al. 2000) for astronomical catalogs.

The field of stellar interiors and evolution accelerated with the introduction of the open-source Modules of Experiments in Stellar Astrophysics (MESA, Paxton et al. 2011,

which currently

57

has over 2500 citations). Computational methods for stellar interiors were first developed half a century before MESA in Iben & Ehrman (1962) and Henyey et al. (1964) based on theory by Chandrasekhar (1938) and Schwarzschild (1958). The computational tools improved in the early 2000 summarized in Lebreton et al. (2008). MESA's publication, Paxton et al. (2011), now has over 2500 citations and led to many improvements and additional software even for gaseous planets in Chen & Rogers (2016). We see a similar evolution in planet interior models.

I describe our planet interior model in Chapter 2. MAGRATHEA at this time is the only open source planet interior model with flexible model parameters. Our transparent structure allows for users to easily modify their models to their desired interior materials and conditions. This makes it a great platform to add functionality and couple various other models. We aim for it to become a community standard for interior modelling.

While, EoS-specific developments are described in Chapter 4. In this chapter, I describe a major update and a add-on that were created after Huang et al. (2022). In Sect. 3.2, I describe a compositional finder which finds interior solutions across 3-layer parameter space for a mass and radius of a planet and is used extensively in later chapters. In Sect. 3.3, I describe an add-on which represents one dimensional MAGRATHEA outputs in three dimensions. In Sec. 3.4, I focus on a list of future development that I aim to complete and partner with other researchers to add to or develop in concert with our interior solver.

3.2 Composition Finder

In the previous chapter in Sec. 2.5.4, I showed on a ternary diagram the range of radii for a given mass of planet with all possible 3-layer interior structures. On Fig. 2.6, you can see lines of

58

Table 3.1: Inputs for the composition finder with line numbers in *main.cpp*.
Variable Details Type Line Number filename File of mass and radius string
302 filename Output file string 334 – OpenMP Options (schedule, num
threads) 343 step Step size of r-cmf double 346 rerr Error tolerance in
simulated radius to target radius double 347 Tgap Temperature of planet and
discontinuities vector 350

constant color which are planets having the same mass and radius. I developed a composition finder routine for MAGRATHEA which given the mass and radius of a planet finds this line of solutions to the interior structure. Furthermore, given observational uncertainties it finds solutions for many draws of mass and radius. I describe the routine here which can be utilized with *input mode=7* in *main.cpp*.

The composition finder takes in a tab separated file of mass and radius samples. These can be generated by fitting a Gaussian or two half-Gaussian to the observed median and standard deviation or can take samples of mass and radius from a observational pipeline. This more realistically captures the distribution of observed mass and radius. Besides simulating the skewness of each value, a combined analysis of mass and radius such as one utilizing transit timing variations will have a correlation between mass and radius. This correlation often is not accounted for in observed interior

studies (e.g. Acuna et al. 2021). I explore the shape of distributions and how they affect ~ inferences of planet composition in Sec. 6.4.1.

In addition to input and output file locations, the finder takes in the inputs from Table 3.1. Mass and radius are stored as double precision variables. The finder outputs the input mass, the mass and radius of each layer of the best fit planet, and the target radius as double variables in a tab separated file.

59

Each mass and radius does not have a unique three-layer solution, so I define the refractory core mass fraction (r-cmf) as the third variable to find solutions. R-cmf is the ratio of the core mass to the non-volatile mass and is given by

$$\text{r-cmf} = \frac{M_{\text{core}}}{M_{\text{mantle}} + M_{\text{core}}} \quad (3.1)$$

or the denominator can equally be expressed as the total mass minus the hydrosphere, $M_{\text{tot}} - M_{\text{hydro}}$. This quantity will be explored graphically in Sec. 6.2. The r-cmf in the case of our simple model with no silicate in the core and no iron in the mantle is equal to the $\frac{\text{Fe}}{\text{Si}+\text{Fe}}$ ratio which may be called the Fe# in geoscience literature. R-cmf ranges from 0 to 1 including 0 and 1 and is not dependent on the hydrosphere mass. For example, Earth and Ganymede have similar r-cmf while Ganymede has half Earth's cmf at 16% (Kuskov & Kronrod 2005).

I sample the r-cmf space uniformly stepping from 1 to 0 in steps corresponding to the variable *step*. I most often use a step of 0.01 or 0.02 leading to 101 or 51 solutions to a

mass and radius input. The solver starts the planet with 100% of the input mass in the core and solves a planet with the given temperatures from T_{gap} using the full MAGRATHEA solver. This gives the smallest radius for a given mass of planet, if the target radius is smaller than this the mass and radius measurement is non-physical for the given planet model. In this case an error is returned and the next mass and radius is solved.

If the target radius is larger than the 100% core planet than 0.1% of the mass is converted to hydrosphere mass and the radius of this new planet is found. I then use a secant method (Papakonstantinou & Tapia 2013) to find the optimal water mass fraction to match the target radius (R_{targ}) with the rest of mass in the core. From the previous two radii (R_i, R_j) at the given water mass

60

fractions ($f_{w,i}, f_{w,j}$), the next water mass fraction ($f_{w,k}$) is found from

$$f_{w,k} = f_{w,j} - (f_{w,j} - f_{w,i})(R_j - R_{targ}) / (R_j - R_i). \quad (3.2)$$

This is repeated until the error in the radius found compared to R_{targ} is within the given value of $rerr$. For an error of 0.1%, the finder takes approximately 5-6 runs. If an error occurs in the MAGRATHEA run an addition 0.01% of mass is converted to hydrosphere and the planet is run again.

The finder is then swept across decreasing r-cmf. The finder begins with cmf equal to r-cmf and the rest of the mass in the mantle. In the second iteration onward after determining the water mass fraction, f_w , to try the core mass fraction, f_c , is given by

$$f_c = r\text{-cmf} * (1 - f_w), (3.3)$$

and the mantle mass fraction, f_m , by

$$f_m = (1 - r\text{-cmf}) * (1 - f_w). (3.4)$$

The optimal water mass fraction is recorded for each r-cmf. When the initial planet's radius with no hydrosphere is larger than the target radius, there are no longer solutions at lower r-cmf and the finder moves to the next mass and radius measurement.

The routine is parallizeable with each mass and radius draw run on a different thread. I can accomplish multithreading with OPENMP (Chandra et al. 2001). The entire routine is currently in *main.cpp*, but will be moved to the back-end with a callable function in *input*

mode=7. 61

With average run times of 1 second and up to 600 runs needed to find solutions at steps of 0.01 in r-cmf for a mass and radius measurement, the finder takes approximately 10 minutes per mass and radius. I often run 5000 posterior input measurements of mass and radius which takes a maximum of 3 days across 12 cores. This scales linearly with step size and with number of inputs.

I use the same finder to assess atmosphere mass fractions. The atmosphere finder has two modes. First the finder can either work exactly as the hydrosphere finder by varying the r-cmf and finding the atmosphere mass as the third layer. The second option is for the user to set a r-cmf and the finder will find the atmosphere mass fraction across

water mass fraction from 0% to 100% water (or a defined cutoff for physically possible water mass fractions).

I use this finder to characterize planet interiors in later chapter with many examples for different planets in Chapter 5 and variations on the Trappist-1 planets in Chapter 6. Previous works which use interior solvers to characterize planets from both mass and radius include Dorn et al. (2015); Santos et al. (2015); Dorn et al. (2017b;a); Brugger et al. (2017); Plotnykov & Valencia (2020); Baumeister et al. (2020) along with many individual observational studies. A majority of these studies use a Markov chain Monte Carlo (MCMC) method to characterize planets.

In the MCMC method, a greater number of model parameters can be explored than mass fraction in each layer. In Dorn et al. (2017b) they use MCMC to constrain the mass fraction of water and atmosphere along with the mantle Fe/Si and Mg/Si ratios.

While we treat these ratios as an unknown space and generate solutions uniformly across this space, the MCMC treatment can take stellar inputs to constrain the probability of interior solutions. However, their more detailed model takes 40-90 seconds to run. In Unterborn et al. (2023), elemental ratios are set in their finder, but these are converted into mass fractions, the input of our code, through simple balances. Acuña et al. (2021) use a MCMC method built on Dorn et al. (2015), but only report the $1-\sigma$ bounds of 62

interior solutions and not the distribution of results. In their models without stellar constraints, I expect their findings are uniform across r-cmf. My method can be more transparent in this case.

3.3 3D Planet Rendering

MAGRATHEA output files provide the radius, pressure, temperature, density, and phase at steps of enclosed mass. Although these results are 1-dimensional, the spherically-symmetric results can be used to visualize the planets in 3-dimensions. Giving the simulated planet interior results a visual representation in 3-dimensions helps our understanding of the volume of each planet material.

Blender is a free and open-source three dimensional software that can be used to create three dimensional models, animations, and simulations. Blender's physics engine allows users to create simulations of physics phenomena, such as fluid dynamics, soft body physics, and particle systems. It's powerful rigid body physics engine can be used to create realistic collisions, gravity, and other physical interactions between objects in a scene. Kent (2013) describes how Blender can be used in a number of astronomy sub-fields. Blender has an embedded Python interpreter that represents all actions in the Python language.

Sri Sudharsan, a high school mentee, and I are using Blender 3.3 to read in a tab separated output file from MAGRATHEA. We sort and record the radii where a phase transition occurs and store these points and name of material in a specified list. We then generate a primitive sphere at the outer radius of the planet and additional shells with a radius corresponding to each phase change. We give each material a specified color, roughness, and texture. We generally use grey/metallic textures for core materials, green or red for mantle, bright red for melted material, and blue for hydrosphere. Green

is chosen for the mantle as a major component of the Earth's upper-mantle is

63

peridotite, a rock composed primarily of green-colored olivine.

The script has the flexibility to generate any planet from the outputs of MAGRATHEA. Running the Python code within the Blender's scripting module will automatically create the planet to scale. We include this open-source package in our GitHub: <https://github.com/DavidRRice/Blender-Magrathea>.

In Fig. 3.1, we show the 3D representation of an Earth-like planet model along with the radial profile of density, pressure, and temperature. The planet is $1 M_{\oplus}$ with a 32.5% core mass fraction. We start the mantle hot at 1800 K assuming a quick temperature rise in the thermally conductive lithosphere and add a 1700 K increase in temperature between the mantle and the core. The planet is made of forsterite, wadsleyite, ringwoodite, bridgmanite, magnesium silicate post-perovskite, liquid iron, and hcp iron. Each of these changes in material is represented by a change in color and texture in the interior.

In Fig. 3.2, we show a collection of planet interiors in 3D. We set up the camera to be the same distance from the planet with the same view, so all planets are to scale relatively in radius. Visible is many phases of water-ice and mantle materials. We use water/ice for the surface if the planet has a hydrosphere depending on the outermost material and a planet texture for the surface if the outermost layer is rock or iron.

Lastly, we are experimenting with coloring the planet by other interior characteristics. To color by a continuous variable, we apply to the sphere a radial "color ramp" for each

layer. Blender color ramps can by default have 32 “color stops”. Thus we read in 32 densities within each layer or within the planet which are evenly spaced in density. We don’t record the exact radius of phase or layer changes, but MAGRATHEA returns more outputs around composition changes to resolve the exact location, so color stops are most often placed near large changes in density.

64

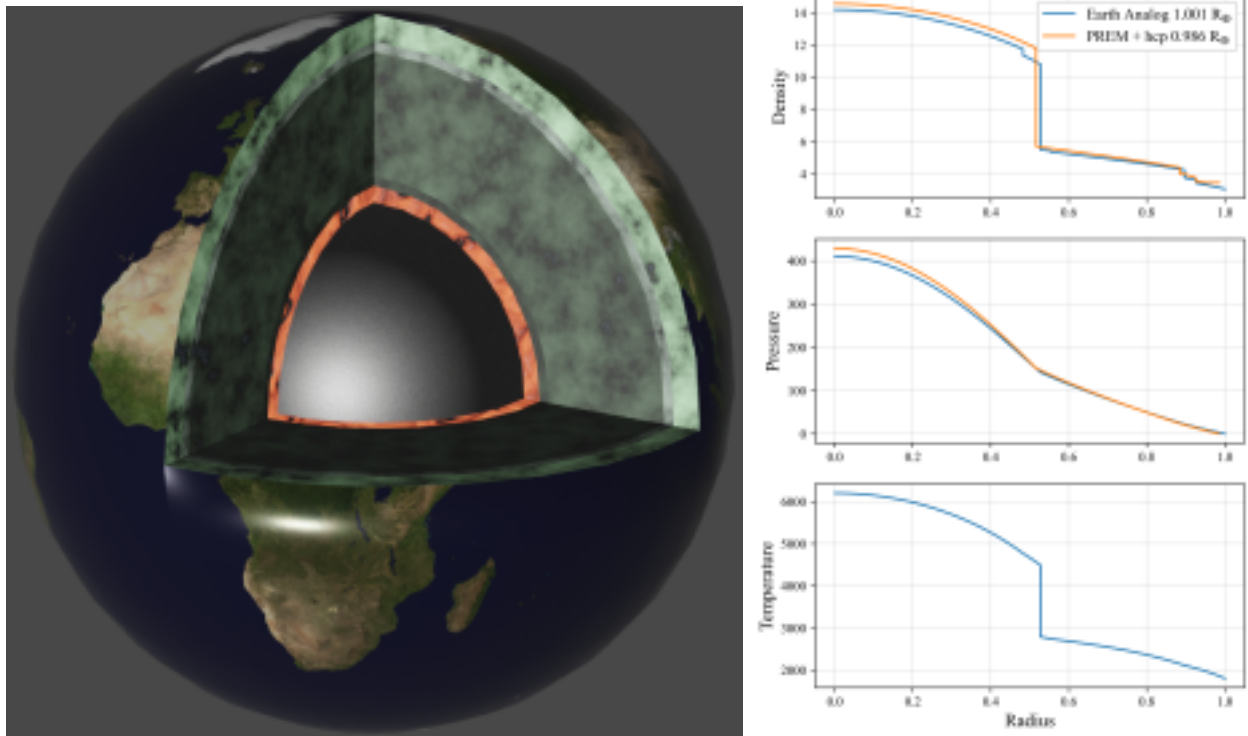


Figure 3.1: *Left*, a Blender rendering of an Earth-like planet with 32.5% of mass in the core with changes in mineralogy marked by changes in color in the interior. *Right*, in *blue* the density, pressure, and temperature of the Earth-like planet compared to a isothermal profile for PREM mantle and hcp-iron core. The radius of discontinuities in density on *top right* correspond with changes in color in 3D *left*.

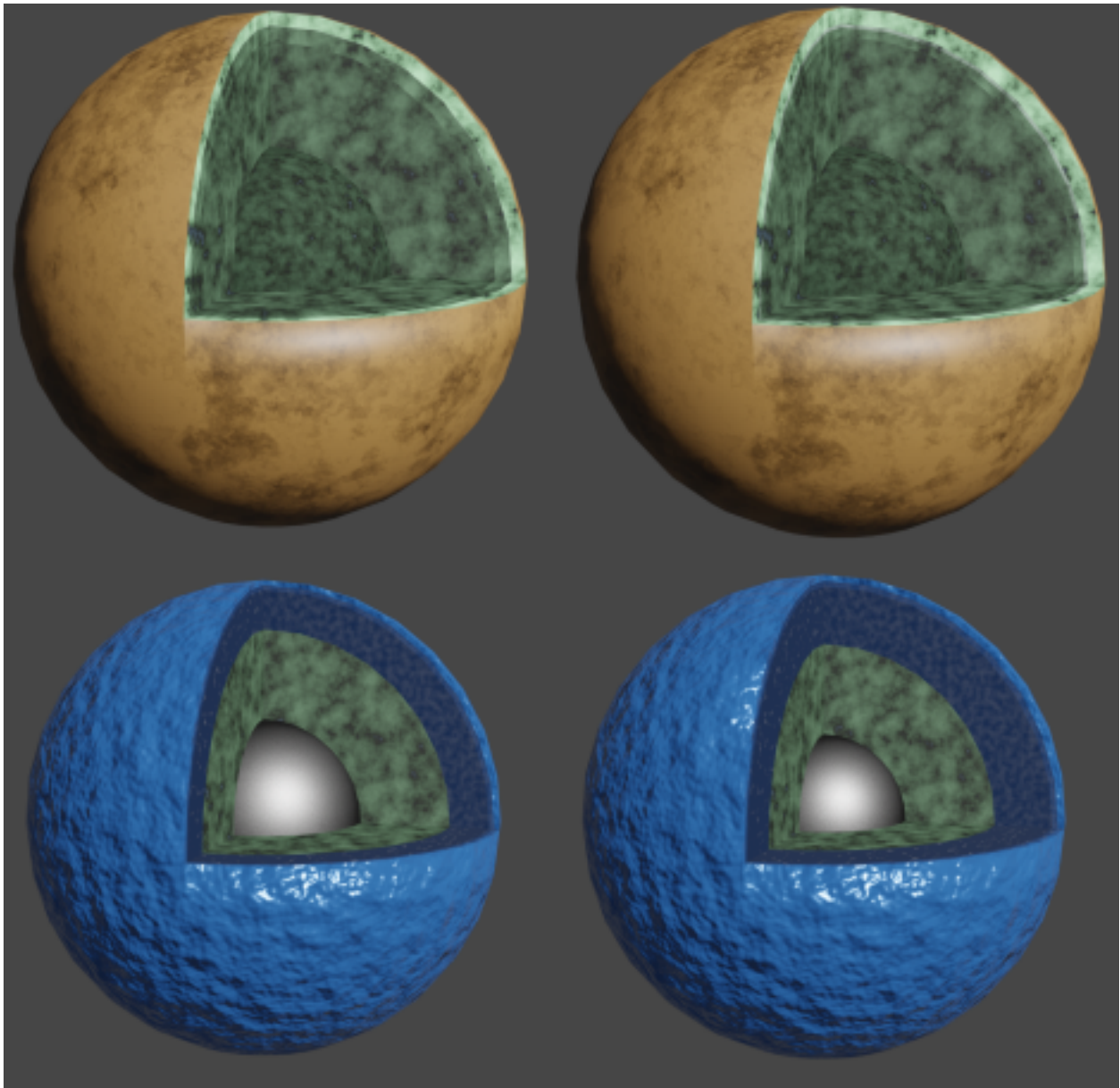


Figure 3.2: *Top*, 100% mantle planets. *Bottom*, planets with significant hydrospheres. *Top left*, planet that is $1 M_{\oplus}$ and $1.07 R_{\oplus}$ surface of 300 K. *Top right*, planet that is $1.1 M_{\oplus}$

and $1.1 R_{\oplus}$ and surface of 1000 K. The second planet's temperature leads to a wds layer shown in green/grey under the olivine layer. *Bottom left*, planet that is $0.63 M_{\oplus}$ and $0.97 R_{\oplus}$ with 42% core. *Bottom, right*, planet that is $0.56 M_{\oplus}$ and $0.99 R_{\oplus}$ with 35% core.

66

To apply the correct color at each location, we find each output density's linear position between a minimum, ρ_{min} , and maximum value, ρ_{max} , for each layer. The position, p , is given by

$$p = \frac{\rho - \rho_{min}}{\rho_{max} - \rho_{min}} \quad (3.5)$$

We read in a Matplotlib colormap and find the color at each of those positions. We add color stops to the Blender colrramp at the radial position given the color and the colrramp interpolates between each output. We show the in-progress rendering in Fig. 3.3.

3.4 Summary and Future Development

In this chapter, I report two major updates to MAGRATHEA's functionality since the publishing of Huang et al. (2022). In Sec. 3.2, I describe my method for finding the range of possible interior structures that are solutions for a single mass and radius measurement. I will use this method extensively to characterize planets in Chapter 5 and Chapter 6. In Sec. 3.3, we take the interior conditions of a planet and represent them in three dimensions. We find this useful for visualizing the volume ratio of different

components.

Looking toward the future we have a number of basic and extensive additions we aim to develop. In MAGRATHEA we prefer empirical fits for the EoS because they are lightweight in terms of storage and parameters can easily be adjusted and tested. However, we do have a two dimensional table input for the EoS. We use these to match the results of Seager et al. (2007). In the future, we plan to develop a three dimensional table interpolator for temperature dependent results also. This is important for inclusion of the AQUA package Haldemann et al. (2020), although their EoSs informing their tables can also be implemented without the use of tables. In addition

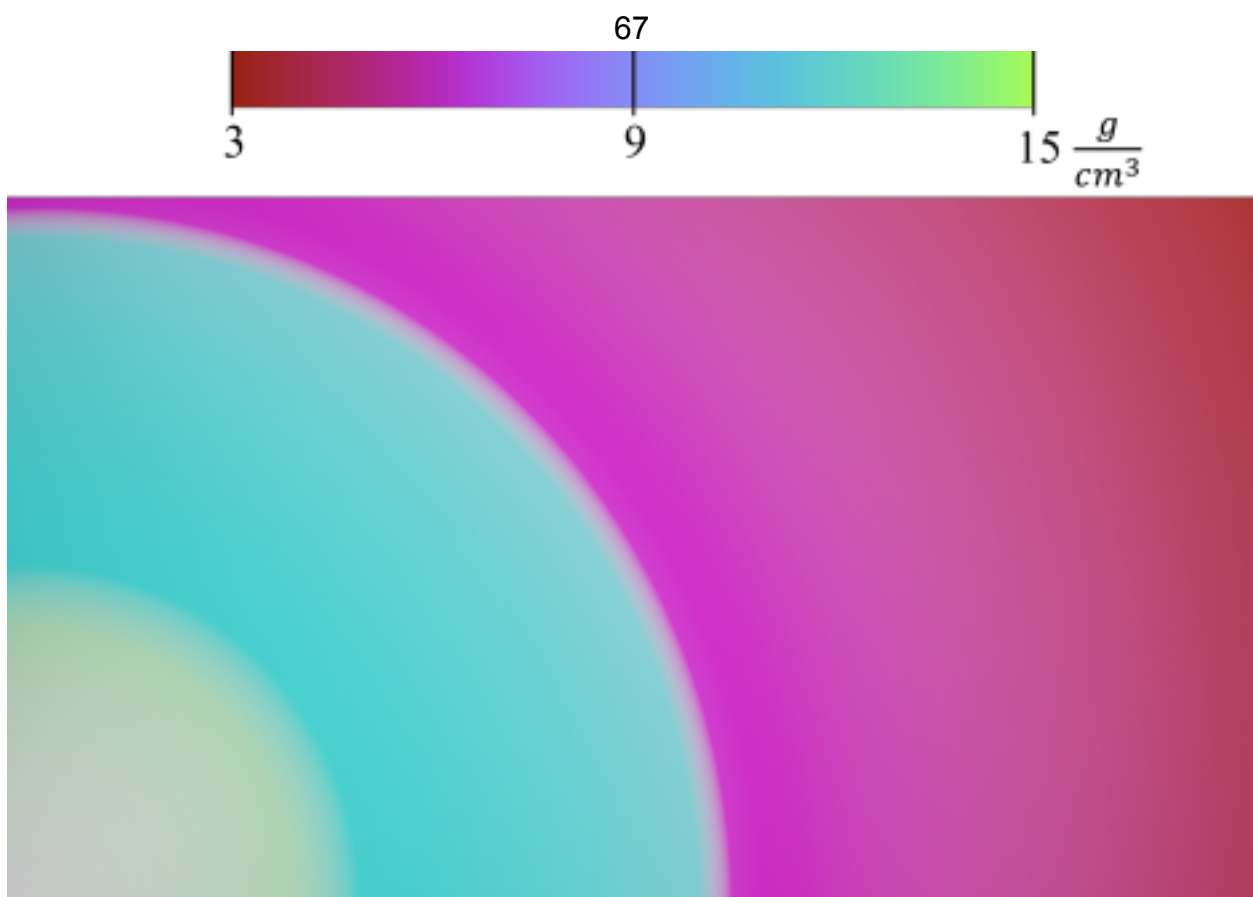


Figure 3.3: The density inside the Earth-like planet in Fig. 3.1. The density increases fairly linearly in the mantle with density jumps in the liquid outer core and solid inner core. The current method does not resolve the upper mantle materials well. Colors are rendered differently in Blender based on lighting and other “material properties” of the

3D sphere so may not correspond exactly to the colorbar.